

Kepler-20: A Sun-like Star with Three Sub-Neptune Exoplanets and Two Earth-size Candidates

Thomas N. Gautier III¹, David Charbonneau², Jason F. Rowe³, Geoffrey W. Marcy⁴, Howard Isaacson⁴, Guillermo Torres², Francois Fressin², Leslie A. Rogers⁵, Jean-Michel Désert², Lars A. Buchhave^{6,7}, David W. Latham², Samuel N. Quinn², David R. Ciardi⁸, Daniel C. Fabrycky⁹, Eric B. Ford¹⁰, Ronald L. Gilliland¹¹, Lucianne M. Walkowicz¹², Stephen T. Bryson³, William D. Cochran¹³, Michael Endl¹³, Debra A. Fischer¹⁴, Steve B. Howell³, Elliott P. Horch¹⁵, Thomas Barclay¹⁶, Natalie Batalha¹⁷, William J. Borucki³, Jessie L. Christiansen³, John C. Geary², Christopher E. Henze³, Matthew J. Holman², Khadeejah Ibrahim³, Jon M. Jenkins¹⁸, Karen Kinemuchi¹⁶, David G. Koch³, Jack J. Lissauer³, Dwight T. Sanderfer³, Dimitar D. Sasselov², Sara Seager⁵, Kathryn Silverio⁴, Jeffrey C. Smith¹⁸, Martin Still¹⁶, Martin C. Stumpe¹⁸, Peter Tenenbaum¹⁸, Jeffrey Van Cleve¹⁸

ABSTRACT

We present the discovery of the Kepler-20 planetary system, which we initially identified through the detection of five distinct periodic transit signals in the *Kepler* light curve of the host star 2MASSJ19104752+4220194. From high-resolution spectroscopy of the star, we find a stellar effective temperature $T_{\text{eff}} = 5455 \pm 100$ K, a metallicity of $[\text{Fe}/\text{H}] = 0.01 \pm 0.04$, and a surface gravity of $\log g = 4.4 \pm 0.1$. We combine these estimates with an estimate of the stellar density derived from the transit light curves to deduce a stellar mass of $M_{\star} = 0.912 \pm 0.034 M_{\odot}$ and a stellar radius of $R_{\star} = 0.944^{+0.060}_{-0.095} R_{\odot}$. For three of the transit signals, we demonstrate that our results strongly disfavor the possibility that these result from astrophysical false positives. We accomplish this

¹Jet Propulsion Laboratory/California Institute of Technology, Pasadena, CA 91109; thomas.n.gautier@jpl.nasa.gov

²Harvard-Smithsonian Center for Astrophysics, Cambridge, MA 02138

³NASA Ames Research Center, Moffett Field, CA 94035

⁴Department of Astronomy, University of California, Berkeley, CA 94720

⁵Massachusetts Institute of Technology, Cambridge, MA 02139

⁶Niels Bohr Institute, University of Copenhagen, DK-2100, Copenhagen, Denmark

⁷Centre for Star and Planet Formation, Natural History Museum of Denmark, University of Copenhagen, DK-1350, Copenhagen, Denmark

⁸NASA Exoplanet Science Institute/California Institute of Technology, Pasadena, CA 91125

⁹Department of Astronomy and Astrophysics, University of California, Santa Cruz, CA 95064

¹⁰Astronomy Department, University of Florida, Gainesville, FL 32111

¹¹Department of Astronomy, 525 Davey Lab, The Pennsylvania State University, University Park, PA 16802

¹²Department of Astrophysical Sciences, Princeton University, Princeton, NJ 08544

¹³McDonald Observatory, The University of Texas at Austin, Austin, TX 78712

¹⁴Department of Astronomy, Yale University, New Haven, CT 06511

¹⁵Department of Physics, Southern Connecticut State University, New Haven, CT 06515

¹⁶Bay Area Environmental Research Institute/NASA Ames Research Center, Moffett Field, CA 94035

¹⁷Department of Physics and Astronomy, San Jose State University, San Jose, CA 95192

¹⁸SETI Institute/NASA Ames Research Center, Moffett Field, CA 94035

by first identifying the subset of stellar blends that reproduce the precise shape of the light curve and then using the constraints on the presence of additional stars from high-angular resolution imaging, photometric colors, and the absence of a secondary component in our spectroscopic observations. We conclude that the planetary scenario is more likely than that of an astrophysical false positive by a factor of 2×10^5 (Kepler-20b), 1×10^5 (Kepler-20c), and 1.1×10^3 (Kepler-20d), sufficient to validate these objects as planetary companions. For Kepler-20c and Kepler-20d, the blend scenario is independently disfavored by the achromaticity of the transit: From *Spitzer* data gathered at $4.5 \mu\text{m}$, we infer a ratio of the planetary to stellar radii of 0.075 ± 0.015 (Kepler-20c) and 0.065 ± 0.011 (Kepler-20d), consistent with each of the depths measured in the *Kepler* optical bandpass. We determine the orbital periods and physical radii of the three confirmed planets to be 3.70 d and $1.91^{+0.12}_{-0.21} R_{\oplus}$ for Kepler-20b, 10.85 d and $3.07^{+0.20}_{-0.31} R_{\oplus}$ for Kepler-20c, and 77.61 d and $2.75^{+0.17}_{-0.30} R_{\oplus}$ for Kepler-20d. From multi-epoch radial velocities, we determine the masses of Kepler-20b and Kepler-20c to be $8.7 \pm 2.2 M_{\oplus}$ and $16.1 \pm 3.5 M_{\oplus}$, respectively, and we place an upper limit on the mass of Kepler-20d of $20.1 M_{\oplus}$ (2σ).

Subject headings: planetary systems — stars: individual (Kepler-20, KIC 6850504, 2MASSJ19104752+4220194) — eclipses

1. Introduction

Systems with multiple exoplanets, and transiting exoplanets, each bolster confidence in the reality of the planetary interpretation of the signals and offer distinct constraints on models of planet formation.

The first extrasolar planets were found around a pulsar (Wolszczan & Frail 1992), and it was the multi-planetary nature — in particular the gravitational perturbations between the planets (Rasio et al. 1992; Wolszczan 1994) — which solidified this outlandish claim. Around Sun-like stars as well, the origin of radial velocity signals continued to be questioned by some, at the time multiple planets were found around ups Andromeda (Butler et al. 1999). The orbital configuration of planets relative to each other has shed light on a host of physical processes, from smooth radial migration into resonant orbits (Lee & Peale 2002) to chaotic scattering into secular eccentricity cycles (Malhotra 2008; Ford et al. 2005). Now with ever-growing statistics of ever-smaller Doppler-detected planets in multiple systems (Mayor et al. 2011), the formation and early history of planetary systems continues to come into sharper focus.

Concurrently, transiting exoplanets have paid burgeoning dividends, starting with the definitive proof that Doppler signals were truly due to gas-giant planets orbiting in close-in orbits (Charbonneau et al. 2000; Henry et al. 2000). Transit lightcurves offer precise geometrical constraints on the orbit of the planet (Winn 2010), such that radial velocity and photometric measurements yield the density of the planet and hence point to its composition (Adams et al. 2008; Miller 2011). Transiting configurations also enable follow-up measurements (Charbonneau et al. 2002; Knutson et al. 2007; Triaud et al. 2010) which inform on the mechanisms of planetary formation, evolution, and even weather.

These two research streams, multiplanets and transiting planets, came together for the first time with the discovery of Kepler-9 (Holman et al. 2010; Torres et al. 2011). This discovery was enabled by data from the *Kepler* Mission (Borucki et al. 2010; Koch et al. 2010), which is uniquely suited for such detections as it offers near-continuous high-precision photometric monitoring of target stars. Based on the first 4 months of *Kepler* data, Borucki et al. (2011) announced the detection of 170 stars each with 2 or more candidate transiting planets; Steffen et al. (2010) discussed in detail 5 systems each possessing multiple candidate transiting planets. A comparative analysis of the population of candidates with multiple planets and single planets was published by Latham et al. (2011), and Lissauer et al. (2011a) discussed the architecture and dynamics of the ensemble of candidate multi-planet systems.

The path to confirming the planetary nature of such *Kepler* candidates is arduous. At present, three stars (in addition to Kepler-9) hosting multiple transiting candidates have been presented in detail and the planetary nature of each of the candidates has been established: These systems are Kepler-10 (Batalha et al. 2011; Fressin et al. 2011a), Kepler-11 (Lissauer et al. 2011b), and Kepler-18 (Cochran et al. 2011). Transiting planets are most profitable when their masses can be determined directly from observation, either through radial velocity (RV) monitoring of the host star or by transit timing variations (TTVs), as was done for Kepler-9bc, Kepler-10b, Kepler-11bcdef, and Kepler-18bcd. When neither the RV or TTV signals is detected, statistical arguments can be employed to show that the planetary hypothesis is far more likely than alternate scenarios (namely blends of several stars containing an eclipsing component), and this was the means by which Kepler-9d, Kepler-10c, and Kepler-11g were all validated. While such work proves the existence of a planet and determines its radius, the mass and hence composition remain unknown save for speculation from theoretical considerations.

This paper presents the discovery of a new system, Kepler-20, with five candidate transiting planets. We validate three of these by statistical argument; we then proceed to use RV measurements to determine the masses of two of these, and we place an upper limit on the mass of the third. We do not validate in this paper the remaining two signals (and hence

remain only candidates, albeit very interesting ones, owing to their diminutive sizes), rather the validation of these two remaining signals is addressed in a separate effort (Fressin et al. 2012). The paper is structured as follows: In §2, we present our extraction of the *Kepler* light curve (§2.1), our modeling of these data (and RVs) to estimate the orbital and physical parameters of the planets and star (§2.2), as well as limits on the motion of the photocentroid during transit (§2.3) and a study of the long-term astrophysical variability of the star from the *Kepler* light curve (§2.4). In §3 we present follow-up observations that we use to argue for the planetary interpretation, including high-resolution imaging (§3.1) and *Spitzer* photometry (§3.2), and the spectroscopy we use to characterize the star and determine the radial velocity signal (§3.3). In §4, we present our statistical analysis that validates the planetary nature of the three largest candidate planets in the system. In §5 we consider the dynamics of the system, and in §6 we discuss the constraints on the composition and formation history of the three planets.

1.1. Nomenclature

Throughout the course of the *Kepler* Mission, a given star is known by many different names (see Borucki et al. 2011, for an explanation of *Kepler* naming conventions), and we pause here to explain the relationship of these names in the current context. The star that is the subject of this paper is located at $\alpha = 19^{\text{h}}10^{\text{m}}47^{\text{s}}.52$, $\delta = +42^{\circ}20'19''.4$ (J2000). It was already known as 2MASSJ19104752+4220194, and in the *Kepler* input catalog it was designated KIC 6850504. After the identification of candidate transiting planets it became a *Kepler* Object of Interest (KOI) and was further dubbed K00070, and it appeared as such in the list of candidates published by Borucki et al. (2011). Some authors have elected to denote KOIs using a different nomenclature, in which case K00070 would be identified as KOI-70. After the confirmation of the planetary nature of three of these candidates it was given its final moniker Kepler-20. This paper describes that process of confirmation, but for simplicity we refer to the star as Kepler-20 throughout. The three confirmed exoplanets were initially assigned KOI designations representing the chronological order in which the transiting signals were identified, but to avoid confusion we will refer to them henceforth by their Kepler-20 designations in which they are ordered by increasing orbital period P ; Kepler-20b (K00070.02, $P = 3.70$ d), Kepler-20c (K00070.01, $P = 10.85$ d), and Kepler-20d (K00070.03, $P = 77.61$ d). We will refer to the two remaining candidates as K00070.04 and K00070.05, but note (as described below) that the period of K00070.04 ($P = 6.10$ d) is intermediate between those of Kepler-20b and Kepler-20c, and the period of K00070.05 ($P = 19.58$ d) is intermediate between those of Kepler-20c and Kepler-20d.

2. Kepler Photometry and Analysis

2.1. Light Curve Extraction

Kepler observations of Kepler-20 commenced UT 2009 May 13 with Quarter 1 (Q1), and the *Kepler* data that we describe here extend through UT 2011 March 14 corresponding to the end of Quarter 8 (Q8), resulting in near-continuous monitoring over a span of 22.4 months. The *Kepler* bandpass spans 423 to 897 nm for which the response is greater than 5% (Van Cleve & Caldwell 2009). This wavelength domain is roughly equivalent to the $V + R$ -band (Koch et al. 2010). These observations have been reduced and calibrated by the *Kepler* pipeline (Jenkins et al. 2010a). The *Kepler* pipeline produces calibrated light curves referred to as Simple Aperture Photometry (SAP) data in the *Kepler* archive, and this is the data product we used as the initial input for our analysis to determine the system parameters (see below). The pipeline provides time series with times in Barycentric Julian Days (BJD), and flux in photo-electrons per observation. The data were initially gathered at long cadence (Caldwell et al. 2010; Jenkins et al. 2010b) consisting of an integration time per data point of 29.426 minutes. After the identification of candidate transiting planets in the data from Q1, the target was also observed at short cadence (Gilliland et al. 2010) corresponding to an integration time of 1 minute for Q2–Q6. We elected to use the long cadence version of the entire Q1–Q8 time series for computational efficiency. There are 29,595 measurements in the Q1–Q8 time series. The upper panel of Figure 1 shows the raw *Kepler* Q1–Q8 light curve of Kepler-20. The data are available electronically from the Multi Mission Archive at the Space Telescope Science Institute (MAST) Web site¹.

2.2. Derivation of System Parameters

The five candidate transiting planets that are the subject of the paper were identified by the procedure described in Borucki et al. (2011). Four of them (Kepler-20b, Kepler-20c, Kepler-20d, K00070.04) are listed in that paper, and K00070.05 was detected subsequently.

We first cleaned the Q1–Q8 long-cadence *Kepler* SAP photometry of Kepler-20 of instrumental and long-term astrophysical variability not related to the planetary transits by fitting and removing a second-order polynomial to each contiguous photometric segment. We defined a segment to be a series of long-cadence observations that does not have a gap larger than five measurements (spanning at least 2.5 hours). In this process, we gave no statistical

¹<http://archive.stsci.edu/kepler>

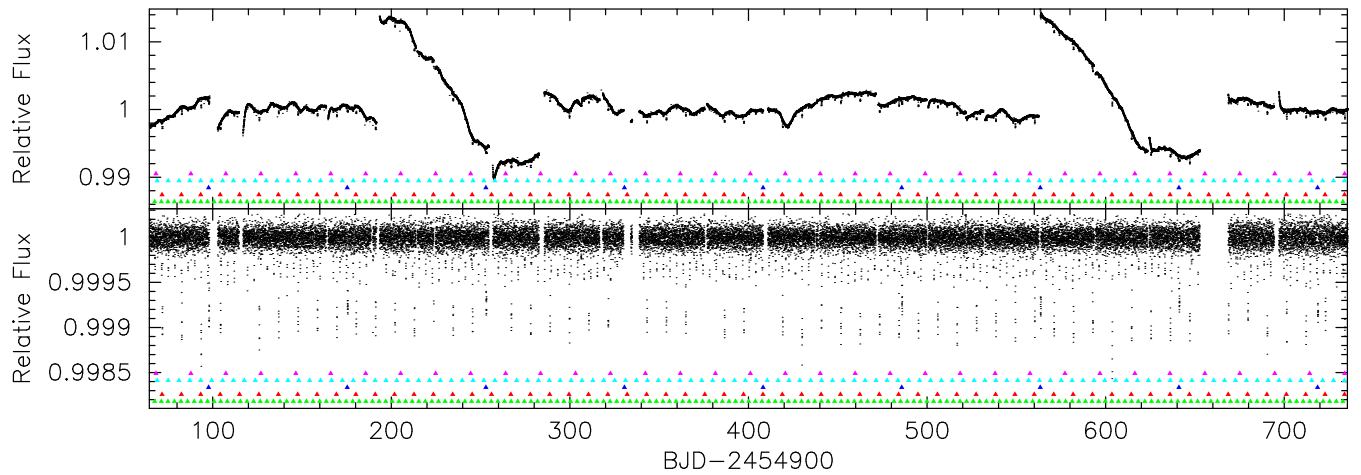


Fig. 1.— *Kepler* light curve of Kepler-20 at a cadence of 30 minutes. *Upper panel:* The normalized raw SAP light curves for Q1–Q8. The star is positioned on one of four different detectors, depending upon the particular quarter, which results in the most obvious offsets that occur roughly 4 times per year. The other discontinuities are due to effects such as spacecraft safe-mode events and loss of fine pointing. *Lower panel:* The SAP light curve after removing instrumental and long-term astrophysical variability via polynomial fitting (see §2.2). In both panels transits of Kepler-20b are marked in green, 20c in red, 20d in blue, K00070.04 in cyan and K00070.05 in magenta.

weight to observations that fell within a transit. We then normalized the corrected light curve by its median, and this cleaned light curve is displayed in the lower panel of Figure 1.

We then modeled simultaneously both this cleaned photometric time series and the radial-velocity measurements (described below in §3.3, and listed in Table 5) to estimate the orbital and physical parameters of the star and its candidate planets. The free parameters in the fit were the mean stellar density ρ_\star and the radial velocity instrumental zero point γ , and 7 parameters for each of the 5 planet candidates $i = \{\text{Kepler-20b, Kepler-20c, Kepler-20d, K00070.04, K00070.05}\}$, namely the epoch of center of transit $T_{0,i}$, the orbital period P_i , the impact parameter b_i , the ratio of the planetary and stellar radii $(R_p/R_\star)_i$, the radial velocity semi-amplitude K_i , and the two quantities, $(e \cos \omega)_i$ and $(e \sin \omega)_i$, relating the eccentricity e_i and the argument of pericenter ω_i . The ratios of the semi-major axes to the stellar radius, $(a/R_\star)_i$, were calculated from ρ_\star and the orbital periods P_i assuming $e = 0$ and that $M_\star \gg$ sum of the planet masses. (We note that our observations do not constrain the eccentricity, but we include it so that our error estimates of the other parameters are inflated to account for this possibility. Similarly, we are not able to detect the radial-velocity signals K_i for Kepler-20d, K00070.04, or K00070.05, but by including these parameters, we include any inflation these may imply for the uncertainties on the mass estimates of Kepler-20b and Kepler-20c, and the upper limit on the mass of Kepler-20d.)

We computed each transit shape using the analytic formulae of Mandel & Agol (2002). We adopted a fourth-order non-linear limb-darkening law with coefficients fixed to those presented by Claret & Bloemen (2011) for the *Kepler* bandpass using the parameters T_{eff} , $\log g$, and $[\text{Fe}/\text{H}]$ determined from spectroscopy (§3.3). Our approach implicitly assumes that all 5 transit signals are due to planets orbiting Kepler-20; the validation of the 3 largest planets, Kepler-20b, Kepler-20c, and Kepler-20d, is presented in §4. Using the validation approach presented in §4, we are not able to validate the remaining two candidates K00070.04 and K00070.05. Instead this difficult problem is deferred to a subsequent study (Fressin et al. 2012). We further assumed that the planets followed non-interacting Keplerian orbits, and that the eccentricity of each planetary orbit was constrained to be less than the value at which it would cross the orbit of another planet, $e \leq 0.396$ (Kepler-20b), 0.319 (Kepler-20c), 0.601 (Kepler-20d), 0.283 (K00070.04), and 0.325 (K00070.05). Finally, we included an additional error term on the radial velocities (beyond those appearing in Table 5) with a typical amplitude of 2 m s^{-1} , to assure that we were not underestimating the uncertainties on the radial velocities (and hence the planetary masses).

We included a prior on ρ_\star as follows. We matched the spectroscopically-estimated T_{eff} , $\log g$, and $[\text{Fe}/\text{H}]$ and the corresponding error estimates (see §3.3) to the Yonsei-Yale evolution tracks (Yi et al. 2001; Demarque et al. 2004) with a Markov-Chain Monte Carlo

(MCMC) routine to produce posterior distributions of stellar mass M_\star and stellar radius R_\star which in turn we used to generate the prior on ρ_\star used for the determination of the best-fit model. The posterior distributions of $(a/R_\star)_i$ were obtained by calculating $(a/R_\star)_i$ for each element of the Markov chain.

We identified the best-fit model by minimizing the χ^2 statistic using a Levenberg-Marquardt algorithm. We estimated the uncertainties via the construction of a co-variance matrix (these results were also used below in the estimate of the width of the Gibbs sample for our MCMC analysis). We then adopted the best-fit model (and its estimated uncertainties) as the seed for an MCMC analysis to determine the posterior distributions of all the model parameters. We used a Gibbs sampler to identify new jump values of test parameter chains by drawing from a normal distribution. The width of the normal distribution for each fitted parameter was initially determined by the error estimates from the best-fit model. We generated 500 elements in the chain and then stopped to examine the success rate, and then were scaled the normal distributions using Equation 8 from Gregory (2011). We repeated this process until the success rate for each parameter fell between 22–28%. We then held the width of the normal distribution fixed.

To handle the large correlation between the model parameters, we adopted a hybrid MCMC algorithm based on Section 3 of Gregory (2011). The routine works by randomly using a Gibbs sampler or a buffer of previously computed chain points to generate proposals for a jump to a new location in the parameter space in a manner similar to the DE-MC algorithm (Ter Braak 2006). The addition of the buffer allows for a calculation of vectorized jumps, which permits efficient sampling of highly correlated parameter space. Once the proposals drawn from the buffer reached an acceptance rate that fell between 22 – 28%, we held the buffer fixed. With the widths of the Gibbs sampler and buffer contents stabilized, we generated 4 chains, each with 1,000,000 elements. The generation of 4 separate chains permitted us to test for convergence via a Gelman-Rubin test.

We adopted the median of the posterior distribution of each parameter as our estimate of its value, and we assigned the uncertainties by identifying the adjacent ranges of each parameter that encompassed 34% of the values above and below the median. We estimated the parameter distributions for the planetary masses and radii by combining the stellar mass and radius distributions from the evolution track fits with the model parameter distributions. The parameter estimates for the star are listed in Table 1, and the parameter estimates for the confirmed planets Kepler-20b, Kepler-20c, and Kepler-20d are listed in Table 2. The light curves phased to the times of transit of each planet or candidate are shown in Figure 2. In Figure 3 we show the radial velocities phased to the orbital periods of Kepler-20b and Kepler-20c.

We note that the values of a/R_* for K00070.04 and K00070.05 were misstated in Table 1 of Fressin et al. (2012). The correct values are $14.4_{-1.2}^{+1.4}$ and $31.3_{-2.5}^{+3.0}$, respectively. The values of the stellar parameters were also stated incorrectly in the same table, and should read $T_{\text{eff}} = 5455 \pm 100 \text{ K}$, $\log g = 4.4 \pm 0.1$, $[\text{Fe}/\text{H}] = +0.01 \pm 0.04$, $v \sin i < 2 \text{ km s}^{-1}$, and $L/L_{\odot} = 0.71_{-0.29}^{+0.14}$. These changes have no effect on the conclusions of Fressin et al. (2012).

Table 1. Parameters for the Star Kepler-20.

Parameter	Value	Notes
Right Ascension (J2000)	19 ^h 10 ^m 47 ^s .52	
Declination (J2000)	+42°20′19″.4	
<i>Kepler</i> Magnitude	12.498	
r Magnitude	12.423	
<i>Spectroscopically Determined Parameters</i>		
Effective temperature T_{eff} (K)	5455 ± 100	A
Spectroscopic gravity $\log g$ (cgs)	4.4 ± 0.1	A
Metallicity [Fe/H]	0.01 ± 0.04	A
Mt. Wilson S-value	0.183 ± 0.005	A
$\log R'_{\text{HK}}$	−4.93 ± 0.05	A
Projected rotation $v \sin i$ (km s ^{−1})	< 2	A
Mean radial velocity (km s ^{−1})	−21.87 ± 0.96	A
Radial Velocity Instrumental Zero Point γ (m s ^{−1})	−3.54 ^{+0.68} _{−1.02}	B
<i>Derived stellar properties</i>		
Mass M_{\star} (M_{\odot})	0.912 ± 0.034	C
Radius R_{\star} (R_{\odot})	0.944 ^{+0.060} _{−0.095}	C
Density ρ_{\star} (cgs)	1.51 ± 0.38	C
Luminosity L_{\star} (L_{\odot})	0.71 ^{+0.14} _{−0.29}	C
Age (Gyr)	8.8 ^{+4.7} _{−2.7}	C
Distance (pc)	290 ± 30	C

Note. — A: Based on the spectroscopic analysis (§3.3).
 B: Not a physical parameter, reported here for completeness.
 C: Based on a comparison of stellar evolutionary tracks to constraints from the spectroscopically-determined parameters (§3.3) and the transit durations (§2.2).

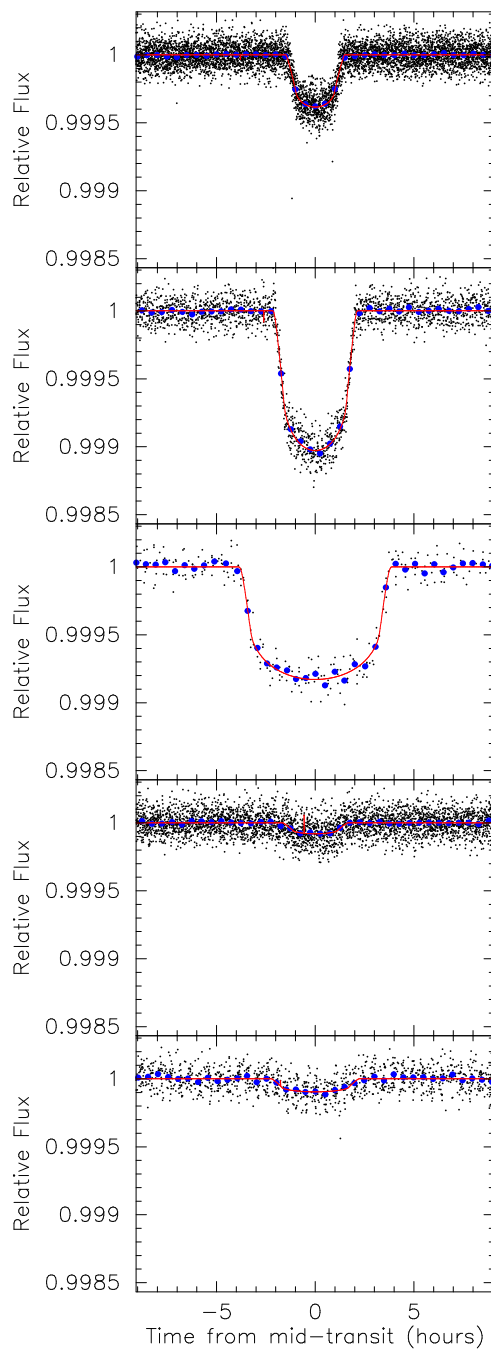


Fig. 2.— *Kepler* light curves with an observational cadence of 30 minutes (*black points*) of Kepler-20, phased to each of the periods of the 5 candidate transiting planets (only data in the vicinity of each phased transit are shown). Kepler-20b, 20c, 20d, K00070.04 and K00070.05 are shown from top to bottom. Blue points with error bars show these measurements binned in phase in increments of 30 minutes. The red curve shows the global best-fit model (see §2.2), which includes smoothing to match this 30 minute cadence.

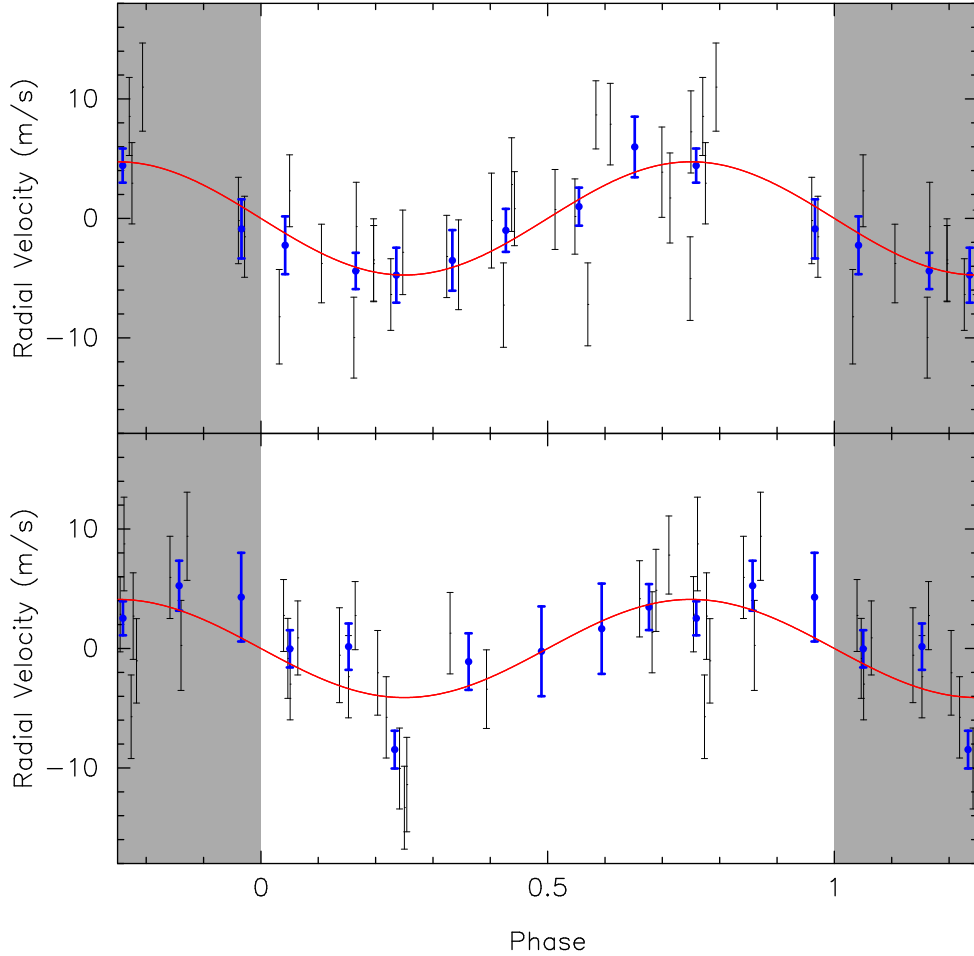


Fig. 3.— *Upper Panel:* Radial velocities of Kepler-20 after correcting for the best-fit amplitudes of Kepler-20b, Kepler-20d, K00070.04, and K00070.05, leaving the effect of only Kepler-20c and plotted as a function of its orbital phase of Kepler-20c. Individual measurements as shown as gray points and these values binned in increments of 0.1 phase units are shown in blue. The phase coverage is extended by 0.25 phase units on either side to show data continuity, but it should be noted the values in these gray regions are plotted twice. The red curve is the best-fit model for the radial velocity variation of the star after the subtraction of the effect of Kepler-20b, Kepler-20d, K00070.04, and K00070.05. *Lower Panel:* Same as above, but showing the radial velocities (in gray, with binned points in blue) and model (in red) of Kepler-20 after correcting for effect of Kepler-20c, Kepler-20d, K00070.04, and K00070.05, leaving the effect of only Kepler-20b and plotted as a function of its orbital phase.

Table 2. Physical and orbital parameters for Kepler-20b, Kepler-20c, and Kepler-20d

Parameter	Kepler-20b	Kepler-20c	Kepler-20d	Notes
Orbital period P (days)	$3.6961219^{+0.0000043}_{-0.0000064}$	10.854092 ± 0.000013	$77.61184^{+0.00015}_{-0.00037}$	A
Midtransit time T_0 (BJD)	$2454967.50027^{+0.00058}_{-0.00068}$	$2454971.60758 \pm 0.00046$	$2454997.7271^{+0.0016}_{-0.0019}$	A
Scaled semi-major axis a/R_\star	$10.29^{+0.97}_{-0.83}$	$21.1^{+2.0}_{-1.7}$	$78.3^{+7.4}_{-6.3}$	A
Scaled planet radius R_p/R_\star	$0.01855^{+0.00026}_{-0.00031}$	0.02975 ± 0.00032	$0.02670^{+0.00046}_{-0.00069}$	A
Impact parameter b	$0.633^{+0.025}_{-0.021}$	$0.594^{+0.018}_{-0.021}$	$0.588^{+0.041}_{-0.032}$	A
$e \cos(\omega)$	$-0.004^{+0.033}_{-0.055}$	$-0.097^{+0.054}_{-0.072}$	$-0.002^{+0.025}_{-0.045}$	A
$e \sin(\omega)$	$-0.021^{+0.021}_{-0.030}$	$-0.011^{+0.031}_{-0.022}$	$-0.007^{+0.025}_{-0.022}$	A
Orbital inclination i (deg)	$86.50^{+0.36}_{-0.31}$	$88.39^{+0.16}_{-0.14}$	$89.570^{+0.043}_{-0.048}$	A
Orbital eccentricity e	< 0.32	< 0.40	< 0.60	A
Orbital semi-amplitude K (m s^{-1})	$3.72^{+0.76}_{-1.09}$	$4.83^{+1.03}_{-0.98}$	$1.2^{+1.0}_{-1.3}$	A
Mass M_p (M_\oplus)	$8.7^{+2.1}_{-2.2}$	$16.1^{+3.3}_{-3.7}$	< 20.1 (2σ)	B
Radius R_p (R_\oplus)	$1.91^{+0.12}_{-0.21}$	$3.07^{+0.20}_{-0.31}$	$2.75^{+0.17}_{-0.30}$	B
Density ρ_p (g cm^{-3})	$6.5^{+2.0}_{-2.7}$	$2.91^{+0.85}_{-1.08}$	< 4.07	B
Orbital semi-major axis a (AU)	$0.04537^{+0.00054}_{-0.00060}$	0.0930 ± 0.0011	$0.3453^{+0.0041}_{-0.0046}$	B
Equilibrium temperature T_{eq} (K)	1014	713	369	C

Note. — A: Based on the joint modeling (§2.2) of the light curve and radial velocities, with eccentricities constrained to avoid orbit crossing.

B: Based on the results from A and estimates of M_\star and/or R_\star from Table 1.

C: Calculated assuming a Bond albedo of 0.5 and isotropic re-radiation of absorbed flux from the entire planetary surface.

2.3. Limits on Motion of Photocentroid

While the analysis above provides the parameter estimates of the five planet candidates under the assumption that each are planets orbiting Kepler-20, it does not address the concern that some or all of these five candidates result instead from an astrophysical false positive (i.e. a blend of several stars within the *Kepler* photometric aperture, containing an eclipsing component). In §4 we use the BLENDER method to demonstrate that this possibility is extremely unlikely for Kepler-20b, Kepler-20c, and Kepler-20d, and it is this BLENDER work that is the basis for our claim that each of these three objects are planets. Another means to identify astrophysical false positives is to examine the *Kepler* pixel data to detect the shift in the photocentroid of the image (e.g. Batalha et al. 2010; Torres et al. 2011; Ballard et al. 2011) of Kepler-20 during times of transit, which we discuss below. Although we do not use the results presented below as part of the BLENDER work, we include a description of it here as it provides an independent argument against the hypothesis that the photometric signals result from an astrophysical false positive and not from planetary companions to Kepler-20.

We use two methods to examine the *Kepler* pixel data to evaluate the location of the photocenter and thus to search for astrophysical false positives: (1) the direct measurement of the source location via difference images, the PRF centroid method, and (2) the inference of the source location from photocenter motion associated with the transits, the flux weighted centroid method. In principle both techniques are similarly accurate, but in practice the flux weighted centroid technique is more sensitive to noise for low signal-to-noise ratio (SNR) transits. We use both techniques because they are both subject to biases due to various systematics, but respond to those systematics in different ways.

In our difference image analysis (Torres et al. 2011), we evaluate the difference between average in-transit pixel images and average out-of-transit images. In the absence of pixel-level systematics, the pixels with the highest flux in the difference image will form a star image at the location of the transiting object, with amplitude equal to the depth of the transit. A fit of the *Kepler* pixel response function (PRF, Bryson et al. 2010) to both the difference and out-of-transit images provides the offset of the transit source from Kepler-20. We measure difference images separately in each quarter, and estimate the transit source location as the robust uncertainty-weighted average of the quarterly results.

We measure photocenter motion by computing the flux-weighted centroid of all pixels downlinked for Kepler-20, generating a centroid time series for row and column. We fit the modeled transit to the whitened centroid time series transformed into sky coordinates. We perform a fit for each quarter, and infer the source location by scaling the difference of these two centroids by the inverse of the flux as described in Jenkins et al. (2010c).

Both the difference image and photocenter motion methods are vulnerable to various systematics, which may bias the result. The PRF fit to the difference and out-of-transit pixel images is biased by PRF errors described in Bryson et al. (2010). The photocenter technique is biased by stars not being completely captured by the available pixels. These types of biases will vary from quarter to quarter. Both methods are vulnerable to crowding, depending on which pixels are downlinked, which varies from quarter to quarter. We ameliorate these biases by taking the uncertainty-weighted robust average of the source locations over available quarters. Because the biases of these difference image and photocenter motion techniques differ, we take agreement of the multi-quarter averages as evidence of that we have faithfully measured the source location of the transit signal.

Table 3 provides the offsets of the transit signal source from Kepler-20 averaged over Q1–Q7 for all five planet candidates. The quarterly measurements and averages for the PRF centroid method are shown in Figure 4. All the average offsets are within 2 sigma of Kepler-20.

Table 3. Offsets between Photocenter of Transit Signal and Kepler-20

Candidate	PRF Centroid [<i>arcsec</i>]	Significance ^a	Flux-weighted Centroid [<i>arcsec</i>]	Significance ^a
Kepler-20b	0.071 ± 0.25	0.29	0.41 ± 0.24	1.72
Kepler-20c	0.021 ± 0.17	0.12	0.072 ± 0.22	0.32
Kepler-20d	0.69 ± 0.74	0.92	3.07 ± 1.96	1.59
K00070.04	0.24 ± 0.51	0.47	2.14 ± 1.79	1.20
K00070.05	0.73 ± 0.45	1.62	1.76 ± 1.91	0.93

^aoffset/uncertainty

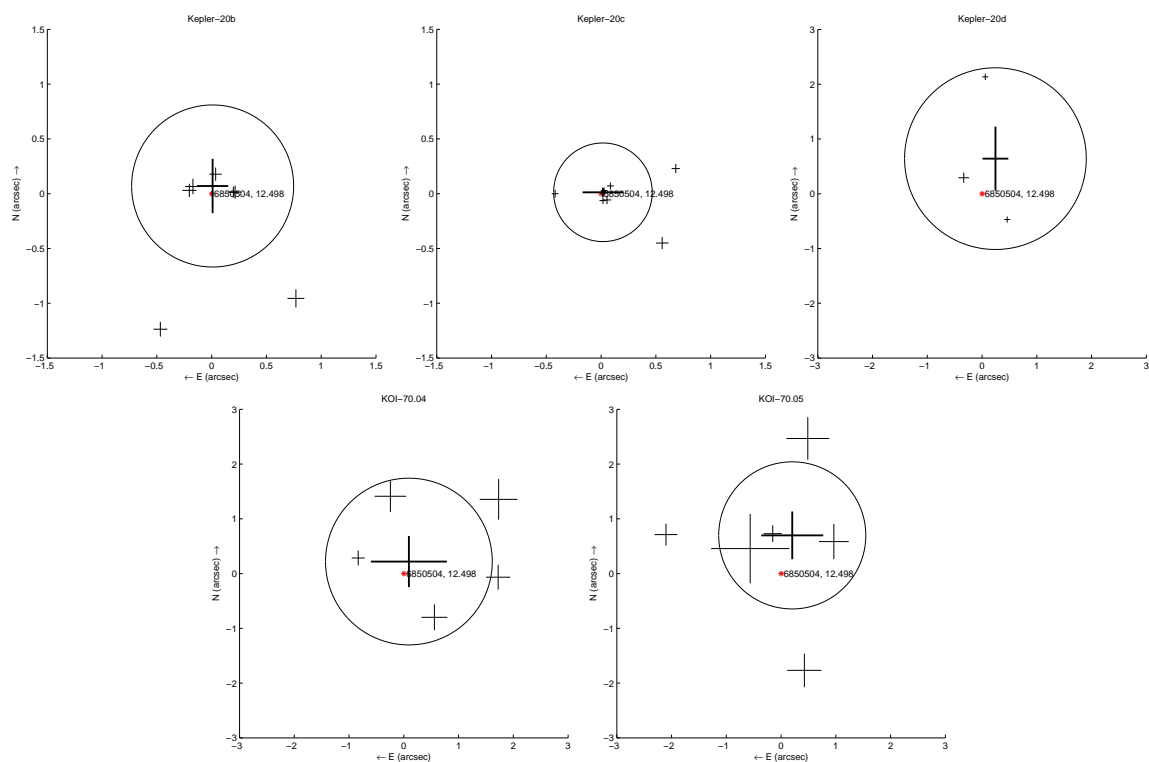


Fig. 4.— Quarterly and average source locations using the difference image (PRF centroid) method for Kepler-20b (top row left), Kepler-20c (top row center), Kepler-20d (top row right), K00070.04 (bottom row left), and K00070.05 (bottom row right). The light crosses show the individual quarter measurements and the heavy crosses show the uncertainty-weighted robust average. The length of the crosses show the 1σ uncertainty of each measurement in RA and Dec. The circles have radius 3σ and are centered at the average measured source location. The location of Kepler-20 is shown by the red asterisk and labeled with its KIC number. In all the panels, the offset between the measured source location and the target is less than 2σ .

2.4. Stellar Activity and Rotation from the *Kepler* Light Curve

While the polynomial-fitting approach in §2.2 is well-suited to cleaning the time series for the transit analysis, it annihilates any long-term variability, such as that due to rotationally modulated star spots. Subsequent to the analysis in §2.2, we obtained a version of the *Kepler* photometry from Q1–Q8 using the new pipeline PDC-MAP (Jenkins et al. 2011), which more effectively removes non-astrophysical systematics in the photometry while leaving the stellar variability intact. We used this PDC-MAP corrected light curve to evaluate the rotational period and stellar activity of the star. We computed a Lomb-Scargle periodogram, and found the highest power peak at a period of 25 days, with a lobe on that peak at around 26 days. This peak is also accompanied by significant power at periods between 24 and 32 days. The distribution of periodicities and in particular the lobed, broad appearance of the peak with the highest power is strongly reminiscent of the activity behavior of the Sun, where differential rotation is responsible for a range of periods from approximately 25 days at the equator to 34 days at the poles. Indeed, the amplitude of spot-related variability on Kepler-20 is very similar to that of the active Sun, as measured during the 2001 season by the SOHO Virgo instrument. Using the SOHO light curves treated to resemble Kepler photometry (as described in Basri et al. 2011), we compared the amplitude of variability of Kepler-20 and the active Sun; the two light curves (and the Lomb-Scargle periodogram of each) are shown in Figure 5. We found that Kepler-20 has spot modulation roughly 30% higher in amplitude than that of our Sun. Our estimate of the rotation period (above) for Kepler-20 is consistent with both its spectroscopically estimated $v \sin i < 2 \text{ km s}^{-1}$ and an estimate of the rotation period, 31 d, based on its Ca H and K emission $\log R'_{\text{HK}}$ (see §3.3). Together, the period and variability indicate that Kepler-20 is very similar to (but perhaps somewhat more active than) our own star.

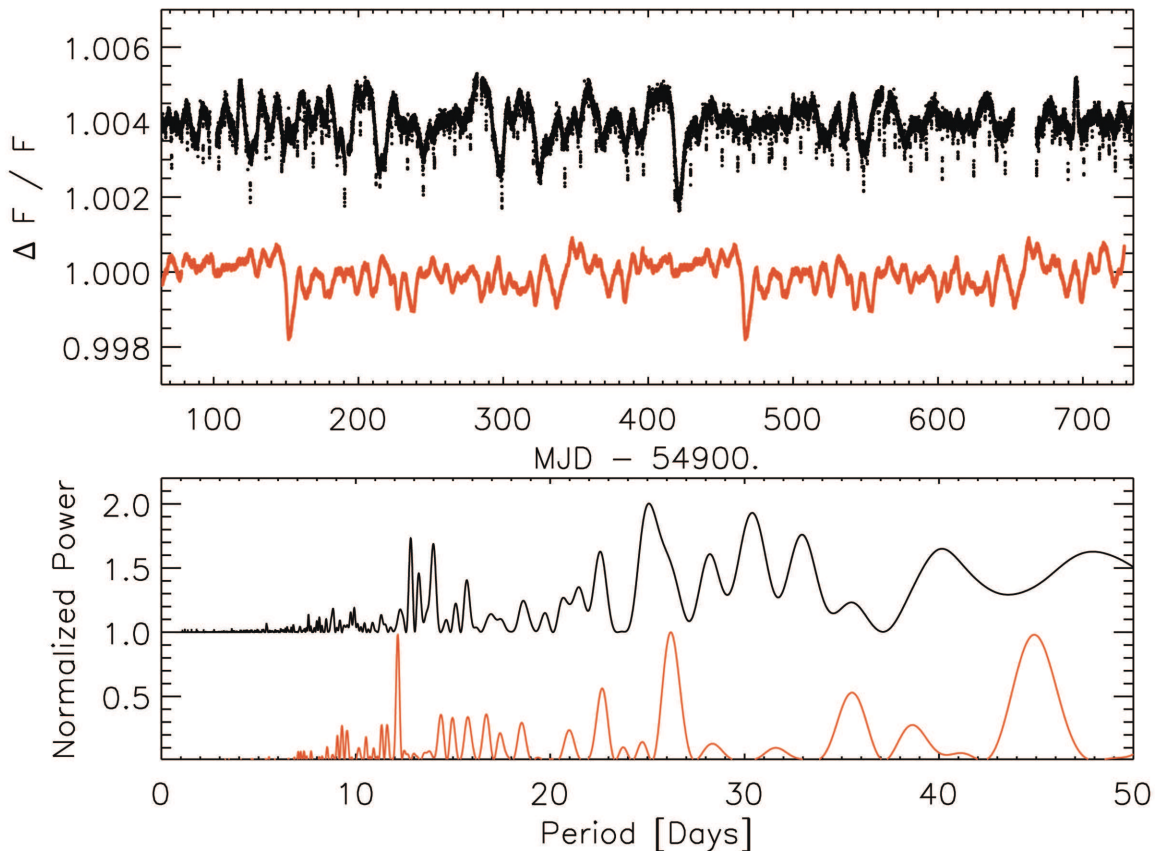


Fig. 5.— *Upper panel:* PDC-MAP corrected lightcurve for Kepler-20 from Q1 to Q8 (black points), showing Kepler-20’s intrinsic stellar variability after removal of instrumental effects. Orange points show the lightcurve for the 2001 active sun from the SOHO Virgo instrument $g + r$ observations for comparison (lightcurve prepared as described in Basri et al. 2010). *Lower panel:* Lomb-Scargle periodogram for each of the two curves appearing in the upper panel.

3. Follow-Up Observations

3.1. High-Resolution Imaging

In order to place limits upon the presence of stars near the target that could be the source of one or more of the transit signals, we gathered high-resolution imaging of Kepler-20 with three separate facilities: We obtained near-infrared adaptive optics images with both the Palomar Hale 5m telescope and the Lick Shane 3m telescope, and we gathered optical speckle observations with the Wisconsin Indiana Yale NOAO (WIYN) 3.5m telescope. Ultimately we used only the Palomar observations in our BLENDER analysis (§4) as these were the most constraining, but we describe all three sets of observations here for completeness.

3.1.1. Adaptive Optics Imaging

We obtained near-infrared adaptive optics imaging of Kepler-20 on the night of UT 2009 September 09 with the Palomar Hale 5m telescope and the PHARO near-infrared camera (Hayward et al. 2001) behind the Palomar adaptive optics system (Troy et al. 2000). We used PHARO, a 1024×1024 HgCdTe infrared array, in 25.1 mas/pixel mode yielding a field of view of $25''$. We gathered our observations in the J ($\lambda_0 = 1.25\mu\text{m}$) filter. We collected the data in a standard 5-point quincunx dither pattern of $5''$ steps interlaced with an off-source ($60''$ East and West) sky dither pattern. The integration time per source was 4.2 seconds at J . We acquired a total of 15 frames for a total on-source integration time of 63 seconds. The adaptive optics system guided on the primary target itself; the full width at half maximum (FWHM) of the central core of the resulting point spread function was $0''.07$.

We further obtained near-infrared adaptive optics imaging on the night of UT 2011 June 17 with the Lick Shane 3m telescope and the IRCAL near-infrared camera (Lloyd et al. 2000) behind the natural guide star adaptive optics system. IRCAL is 256×256 pixel PICNIC array with a plate scale of 75.6 mas/pixel, yielding a total field of view of $19''.6$. We gathered our observations using the K_s ($\lambda_0 = 2.145\mu\text{m}$) filter, and, as with the Palomar observations, we used a standard 5-point dither pattern. The integration time per frame was 120 seconds; we acquired 10 frames for a total on-source integration time of 1200 seconds. The adaptive optics system guided on the primary target itself; the FWHM of the central core of the resulting point spread function were $0.79''$. The final coadded images at J and K_s are shown in Figure 6.

In addition to Kepler-20, we detected two additional sources. The first source is $3''.8$ to the northeast of the target and is fainter by $\Delta J \approx 4.5$ magnitudes and $\Delta K_s \approx 4.2$

magnitudes. The star has an infrared color of $J - K_s = 0.19 \pm 0.02$ mag which yields an expected *Kepler* magnitude of $Kp = 16.1 \pm 0.2$ mag (Howell et al. 2011a). A much fainter source, at $11''$ to the southeast, was detected only in the Palomar J data and is $\Delta J = 8.5$ magnitudes fainter than the primary target. The fainter source, based upon expected stellar $Kp - J$ colors (Howell et al. 2011a), has an expected *Kepler* magnitude of $Kp = 21.0 \pm 0.7$ mag.

No additional sources were detected in the imaging. We determined the sensitivity limits of the imaging by calculating the noise in concentric rings radiating out from the centroid position of the primary target, starting at one FWHM from the target with each ring stepped one FWHM from the previous ring. The 3σ limits of the J -band and K -band imaging were approximately 20 mag and 16 mag, respectively (see Figure 7). The respective J -band and K -band imaging limits are approximately 8.5 and 5.5 mag fainter than the target, corresponding to contrasts in the *Kepler* bandpass of approximately 9 mag and 6.5 mag.

3.1.2. Speckle Imaging

We obtained speckle observations of Kepler-20 at the WIYN 3.5m telescope on two different nights, UT 2010 June 18 and UT 2010 September 17. We gathered both sets of observations with the new dual channel speckle camera described in Horch et al. (2011). On both nights the data consisted of 3 sets of 1000 exposures each with an individual exposure time of 40ms, with images gathered simultaneously in two filters. The data collection, reduction, and image reconstruction process are described in the aforementioned paper as well as in Howell et al. (2011b), and the latter presents details of the 2010 observing season of observations with the dual channel speckle camera for the *Kepler* follow up program.

On both occasions our speckle imaging did not detect a companion to Kepler-20 within an annulus of $0.05 - 1.8$ arcsec from the target. The September observation yielded detection limits of 3.82 (in V) and 3.54 (in R) magnitudes fainter than Kepler-20. The June observation yielded limits of 3.14 and 4.92 fainter in V and R respectively. Therefore we rule out the presence of a second star down to 3.82 magnitudes fainter in V and 4.92 magnitudes fainter in R over an angular distance of $0.05 - 1.8$ arcseconds from Kepler-20.

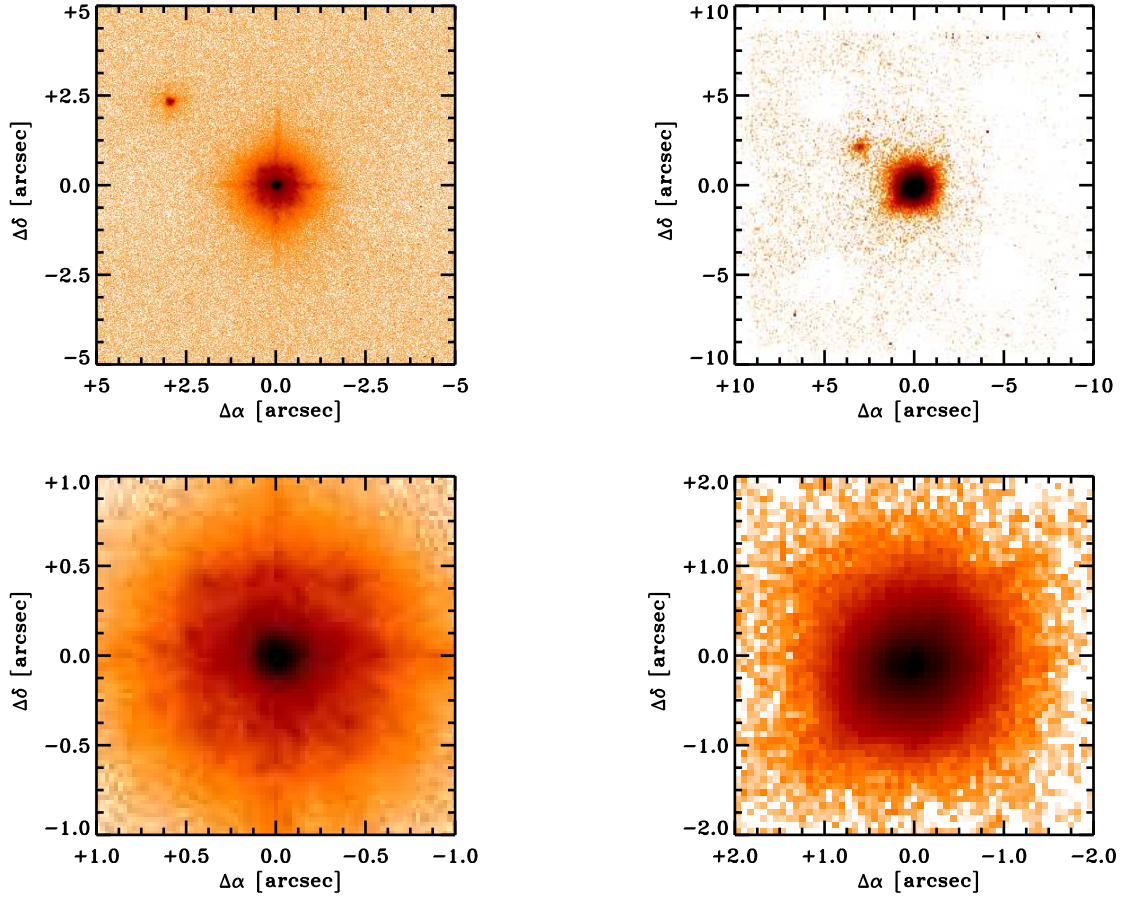


Fig. 6.— Palomar J (left) and Lick K_s (right) adaptive optics images of Kepler-20. The top row displays a $10'' \times 10''$ field of view for the Palomar J image and a $20'' \times 20''$ for the Lick K_s image. The bottom row displays zoomed images highlighting the area immediately around the target .

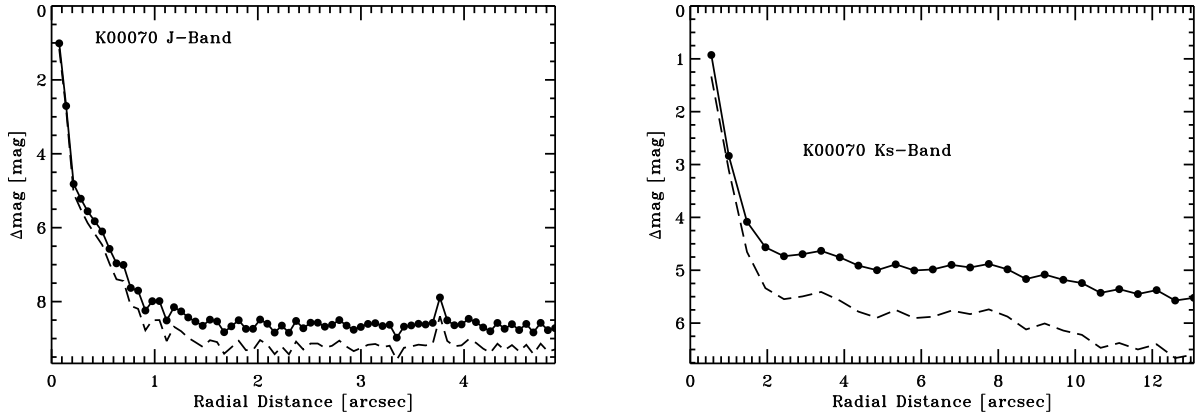


Fig. 7.— *Left panel:* The sensitivity limits of the Palomar J -band adaptive optics imaging are plotted as a function of radial distance from the primary target. The filled circles and solid line represent the measured J -band limits; each filled circle represents one step in FWHM. The dashed line represents the derived corresponding limits in the *Kepler* bandpass based upon the expected $K_p - J$ colors (Howell et al. 2011a). *Right panel:* Same as above, but showing the sensitivity limits of the Lick K_s -band adaptive optics imaging. The dashed line is based upon the expected $K_p - K_s$ colors.

3.2. Photometry with the *Spitzer* Space Telescope

An essential difference between true planetary transits and astrophysical false positives resulting from blends of stars is that the depth of a planetary transit is achromatic (neglecting the small effect of stellar limb-darkening), whereas false positives are not (except in the unlikely case that the effective temperatures of the contributing stars are extremely similar). By providing infrared time series spanning times of transit, the Warm *Spitzer* Mission has assisted in the validation of many transiting planet systems, including Kepler-10 (Fressin et al. 2011a), Kepler-14 (Buchhave et al. 2011), Kepler-18 (Cochran et al. 2011), Kepler-19 (Ballard et al. 2011), and CoRoT-7 (Fressin et al. 2011b). We describe below our observations and analysis of Warm *Spitzer* data spanning transits of Kepler-20c and Kepler-20d, which provide independent support of their planetary nature.

3.2.1. Observations and Extraction of the Warm *Spitzer* Time Series

We used the IRAC camera (Fazio et al. 2004) on board the *Spitzer* Space Telescope (Werner et al. 2004) to observe Kepler-20 spanning one transit of Kepler-20c and two transits of Kepler-20d. We gathered our observations at $4.5\ \mu\text{m}$ as part of program ID 60028. The visits lasted 8.5 hours for Kepler-20c and 16.5 hours for both visits of Kepler-20d. We used the full-frame mode (256×256 pixels) with an exposure time of 12 s per image, which yielded 2451 and 4643 images per visit for Kepler-20c and Kepler-20d, respectively.

The method we used to produce photometric time series from the images is described in Désert et al. (2009). It consists of finding the centroid position of the stellar point spread function (PSF) and performing aperture photometry using a circular aperture on individual Basic Calibrated Data (BCD) images delivered by the *Spitzer* archive. These files are corrected for dark current, flat-fielding, detector non-linearity and converted into flux units. We converted the pixel intensities to electrons using the information given in the detector gain and exposure time provided in the image headers; this facilitates the evaluation of the photometric errors. We adjusted the size of the photometric aperture to yield the smallest errors; for these data the optimal aperture was found to have a radius of 3.0 pixels. We found that the transit depths and errors varied only weakly with the aperture radius for each of the light curves. We used a sliding median filter to identify and trim outliers that differed in flux or positions by greater than $5\ \sigma$. We also discarded the first half-hour of observations, which are affected by a significant jitter before the telescope stabilizes. We estimated the background by fitting a Gaussian to the central region of the histogram of counts from the full array. Telescope pointing drift resulted in fluctuations of the stellar centroid position, which, in combination with intra-pixel sensitivity variations, produces systematic noise in

the raw light curves. A description of this effect, known as the pixel-phase effect, is given in the *Spitzer*/IRAC data handbook (Reach et al. 2006) and is well known in exoplanetary studies (e.g. Charbonneau et al. 2005; Knutson et al. 2008). After correction for this effect (see below) we found that the point-to-point scatter in the light curve indicated an achieved SNR of 220 per image, corresponding to 85% of the theoretical limit.

3.2.2. Analysis of the Warm Spitzer Light Curves

We modeled the time series using a model that was a product of two functions, one describing the transit shape and the other describing the variation of the detector sensitivity with time and sub-pixel position, as described in Désert et al. (2011a). For the transit light curve model, we used the transit routine OCCULTNL from Mandel & Agol (2002). This function depends on the parameters $(R_p/R_\star)_i$, $(a/R_\star)_i$, b_i , and $T_{0,i}$, where $i = \{\text{Kepler-20c, Kepler-20d}\}$, the two candidate planets for which we gathered observations. The contribution of stellar limb-darkening at $4.5 \mu\text{m}$ is negligible given the low precision of our Warm *Spitzer* data and so we neglect this effect. We allow only $(R_p/R_\star)_i$ to vary in our analysis; the other parameters are set to the values derived from the analysis of the *Kepler* light curve (see Table 2). Because of the possibility of transit-timing variations (see §5), we set the values of $T_{0,i}$ to the values measured from *Kepler* for the particular event. Our model for the variation of the instrument response consists of a sum of a linear function of time and a quadratic function (with four parameters) of the x and y sub-pixel image position. We simultaneously fit the instrumental function and the transit shape for each individual visit. The errors on each photometric point were assumed to be identical, and were set to the root-mean-squared residuals to the initial best fit obtained.

To obtain an estimate of the correlated and systematic errors in our measurements, we use the residual permutation bootstrap method as described in Désert et al. (2009). In this method, the residuals of the initial fit are shifted systematically and sequentially by one frame and added to the transit light curve model, which is then fit once again and the process is repeated. We assign the error bars to be the region containing 34% of the results above and 34% of the results below the median of the distributions, as described in Désert et al. (2011b). As we observed two transits of Kepler-20d we further evaluated the weighted mean of the transit depth for this candidate. In Table 4, we provide a summary of the *Spitzer* observations and report our estimates of the transit depths and uncertainties. In Figure 8, we plot both the raw and corrected time series for each candidate, and overplot the theoretical curve expected using the parameters estimated from the *Kepler* photometry (see below).

The adaptive optics images described in §3.1.1 reveal the presence of a star adjacent to Kepler-20. This adjacent star is 4.5 magnitudes fainter in J -band than Kepler-20, and located at an angular separation of $3.8''$, which corresponds to 3.1 IRAC pixels. We tested whether the measured transit depths have to be corrected to take into account the contribution from this stellar companion. We computed the theoretical dilution factor by extrapolating the J -band measurements to the *Spitzer* bandpass at $4.5 \mu\text{m}$. We estimate that 1.6% of the photons recorded during the observation come from the companion star. For a blend of two sources, the polluted transit depth would be $d/(1 + \epsilon)$, where d is the unblended transit depth, and $\epsilon = 1.6\%$. Since the effect on d is well below our detection threshold, we conclude that the presence of the contaminant star near Kepler-20 does not affect our estimates of the transit depths.

We calculate the transit shapes that would be expected from the parameters estimated from the *Kepler* photometry (Table 2) and overplot these on the *Spitzer* time series in Figure 8. The depths we measure with *Spitzer* are in agreement with the depths expected from the *Kepler*-derived parameters at the 1σ level. Our *Spitzer* observations demonstrate that the transit signals of Kepler-20c and Kepler-20d are achromatic, as expected for planetary companions and in conflict with the expectation for most (but not all) astrophysical false positives resulting from blends of stars within the photometric aperture of *Kepler*.

Table 4. Transit Depths at $4.5 \mu\text{m}$ from *Warm Spitzer*

Candidate	AOR Name	Date of Observation [UT]	Data Number	Time of Transit Center [BJD]	Transit Depth(%)
Kepler-20c	r41165824	2010-12-05	2291	2455536.0209	0.075 ± 0.015
Kepler-20d	r39437568	2010-09-24	4451	2455463.4022	$0.063^{+0.019}_{-0.014}$
Kepler-20d	r41164544	2010-12-10	4383	2455540.9925	0.067 ± 0.016
Kepler-20d	weighted mean	–	–	–	0.065 ± 0.011

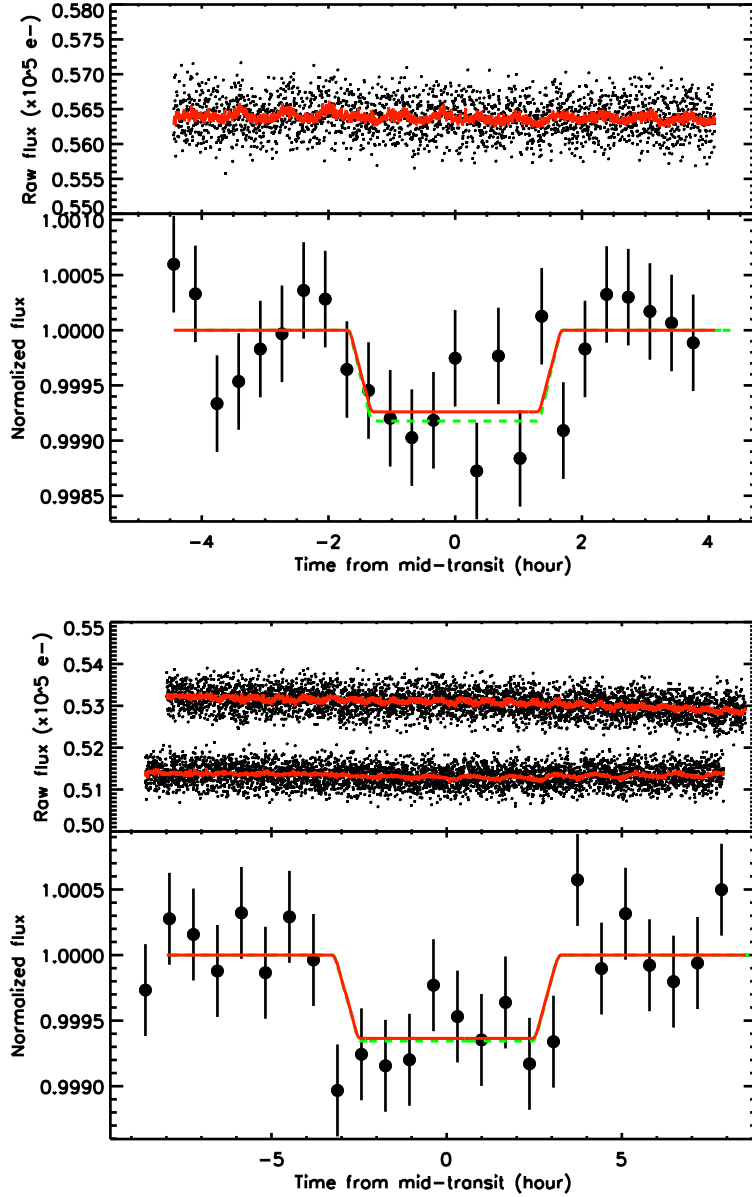


Fig. 8.— Warm *Spitzer* transit light curves of Kepler-20 observed in the IRAC band-pass at $4.5 \mu\text{m}$ spanning times of transit of Kepler-20c (*upper half of figure*) and Kepler-20d (*lower half of figure*). For each candidate, the raw and unbinned time series are shown in the upper panels, and the red solid lines correspond to the best-fit models, which include both the effects of the instrumental variation with time and image position and the planetary transit (see §3.2). In the lower panel for each candidate, we display these data after correcting for the instrumental model, normalizing, and binning by 20 minutes. In the case of Kepler-20d we co-added the two light curves. The best-fit model for the transits are plotted in red and the transit shapes expected from the parameters estimated from the *Kepler* observations (Table 2) are over-plotted as dashed green lines. The transit depths measured in the *Spitzer* and *Kepler* bandpasses agree to better than 1σ .

3.3. Spectroscopy

We obtained 30 high resolution spectra of Kepler-20 between UT 2009 August 30 and 2011 June 16 using the HIRES spectrometer on the Keck I 10-m telescope (Vogt et al. 1994). We took spectra with the same spectrometer set up of HIRES, and with the same spectroscopic analysis, that we normally use for precise Doppler work of nearby FGK stars (Johnson et al. 2011), which typically yields a Doppler precision of 1.5 m s^{-1} for slowly rotating FGKM stars. Typical exposure times ranged from 30–45 minutes, yielding an SNR of 120 per pixel (1.3 km s^{-1}). The first 9 observations were made with the B5 decker ($0''.87 \times 3''.0$) that does not permit moonlight subtraction. The remaining 21 observations were made with the C2 decker ($0''.87 \times 14''.0$) that permits sky subtraction. The internal errors were estimated to be between $1.5\text{--}2 \text{ m s}^{-1}$. We augmented these uncertainties by adding a jitter term of 2.0 m s^{-1} in quadrature. The earlier 9 observations are vulnerable to modest contamination from moonlight, and we have further augmented the uncertainties for these 9 values by adding in quadrature a term of 2.7 m s^{-1} , which is based on the ensemble performance of stars similarly affected for this magnitude. The final uncertainties range from $2.5\text{--}4 \text{ m s}^{-1}$. The estimated RVs and uncertainties are given in Table 5. We also undertook a study of these spectra to determine the spectral line bisectors with the goal of placing limits on these sufficient to preclude astrophysical false positives. However, we found that the scatter in the bisector centers was somewhat larger than the RV variations, rendering the RV detection, while sufficient for mass constraint, inconclusive for confirmation. We therefore undertook the statistical study described in §4).

We obtained two additional spectra of Kepler-20 with HIRES on UT 2009 September 08 and 2010 August 24. These observations were gathered without the iodine cell, so that the extracted stellar spectrum could be used for the template for the RV analysis and for estimating stellar parameters. The exposure time for the first spectrum was 30 minutes yielding a typical SNR of 90 and the B1 decker ($R = 60,000$) was used. The observing conditions were slightly better when the second spectrum was obtained and a one hour exposure yielded a SNR of 140. The taller B3 decker ($R = 60,000$) was used to carry out a better sky subtraction. We analyzed these two spectra using the LTE spectral synthesis analysis software *Spectroscopy Made Easy* (SME; Valenti & Piskunov 1996; Valenti & Fischer 2005) to estimate the values of T_{eff} , $\log g$ [Fe/H] and $v \sin i$. We found that the estimates from each spectrum were consistent to within 1σ , and hence we averaged our two estimates to obtain $T_{\text{eff}} = 5455 \pm 44 \text{ K}$, $\log g = 4.4 \pm 0.1$, [Fe/H] = 0.01 ± 0.04 , and $v \sin i < 2 \text{ km s}^{-1}$; the errors listed are those resulting from the analysis of each individual spectrum, and we have refrained from assuming a decrease by a factor of $\sqrt{2}$. We also proceeded to measure the flux in the cores of the Ca II H and K lines to evaluate the chromospheric activity. We measured that the ratio of emission in these lines to the bolometric emission was $\log R'_{\text{HK}} = -4.93 \pm 0.05$. This

estimate was derived from a Mt. Wilson-style S-value of 0.183 ± 0.005 (Isaacson & Fischer 2010), using the measured color $B - V = 0.725$. The $\log R'_{\text{HK}}$ value suggests a low activity level for a star of this spectral type, which is consistent with the measured $v \sin i < 2 \text{ km s}^{-1}$. Using the relations of Noyes et al. (1984) and Mamajek & Hillenbrand (2008), we infer a rotation period of 31 days.

We also gathered three moderate signal-to-noise ratio, high-resolution spectra of Kepler-20 for reconnaissance purposes, two with the FIBre-fed Échelle Spectrograph (FIES) at the 2.5 m Nordic Optical Telescope (NOT) at La Palma, Spain (Djupvik & Andersen 2010) and one with the Tull Coudé Spectrograph on the McDonald observatory 2.7m Harlan Smith Telescope. The FIES spectra were taken on 2009 August 5 and 6 using the medium and high resolution fibers resulting in a resolution of 46,000 and 67,000, respectively. Each spectrum has a wavelength coverage of approximately 360 – 740 nm. The McDonald spectrum was taken on 2010 October 25, with a spectral resolution of 60,000. This spectrum was exposed to a SNR of 55 per resolution element for the specific purpose of deriving reliable atmospheric parameters for the star.

As an independent check on the parameters derived from the SME analysis of the Keck/HIRES data described above, we derived stellar parameters following Torres et al. (2002) and Buchhave et al. (2010). As part of this analysis, we employed a new fitting scheme that is currently under development by L. Buchhave, allowing us to extract precise stellar parameters from the spectra. We analyzed the two FIES spectra, the McDonald spectrum and the three HIRES template spectra. These results were found to be consistent within the errors. Taking the average of the stellar parameters from the different instruments yielded the following parameter estimates: $T_{\text{eff}} = 5563 \pm 50 \text{ K}$, $\log g = 4.52 \pm 0.10$, $[\text{m}/\text{H}] = +0.04 \pm 0.08$, and $v \sin i = 1.80 \pm 0.50 \text{ km s}^{-1}$, in agreement with the parameters from SME within the uncertainties. The average systemic radial velocity of the six observations was $-21.87 \pm 0.96 \text{ km s}^{-1}$ on the IAU standard scale, which includes the correction for the gravitational redshift of the Sun.

We note that the two analyses yielded consistent results for $\log g$, metallicity, and $v \sin i$, but that the estimates of T_{eff} differed by twice the formal error. Hence we elected to adopt the results of the SME analysis for our final values, but we increased the uncertainty on T_{eff} to 100 K to reflect the difference between the two estimates. We list our estimates for the spectroscopically determined parameters in Table 1.

Table 5. Keck HIRES Radial Velocity Measurements for Kepler-20

Date of Obs. [BJD]	Radial Velocity [m s^{-1}]	Uncertainty [m s^{-1}] ^a
2455073.885713	−5.86	3.78
2455074.861139	−2.94	3.74
2455075.906678	1.09	3.75
2455076.883792	2.57	3.84
2455077.907884	11.08	3.82
2455081.952637	−1.51	3.83
2455082.832587	−9.53	3.78
2455083.888144	−7.17	3.84
2455084.893633	4.59	3.88
2455134.766132	−14.15	3.88
2455314.027873	2.05	2.54
2455320.085390	−9.47	2.59
2455321.072318	−4.55	2.56
2455345.011208	−8.71	2.82
2455351.073218	0.41	2.70
2455352.043110	−1.84	2.50
2455372.898433	1.71	2.62
2455374.967141	−16.20	2.62
2455378.007402	−2.59	2.53
2455380.950103	−0.62	2.55
2455403.055761	7.59	2.96
2455407.903131	−10.15	2.64
2455411.959424	−13.79	2.65
2455413.894286	−2.60	2.59
2455433.818795	4.81	2.46
2455435.841063	10.04	2.58
2455440.792117	−10.94	2.50
2455500.817440	−2.94	3.34
2455522.725846	−6.56	2.63
2455724.055721	−2.35	2.64

^aIncludes jitter of 2 m s^{-1}

4. Validation of the Planets Kepler-20b, Kepler-20c, and Kepler-20d

While the analysis of the radial-velocity (§3.3) data yielded detections for Kepler-20b and Kepler-20c, we found that our analyses of the bisector spans were not sufficient to confirm the planetary origin of those variations. Moreover, for Kepler-20d, K00070.04, and K00070.05 there is no Doppler detection. We therefore rely on a fundamentally different technique to establish which, if any, of these signals can be persuasively attributed to planets. As explained in Lissauer et al. (2011b), when dynamical confirmation of a planet candidate by the radial velocity method or by transit timing variations cannot be achieved, we attempt instead to validate the candidate by tabulating all viable false positives (blends) that could mimic the signal. We then assess the likelihood of these blends, and compare it with an *a priori* estimate of the likelihood that the signal is due to a true planet. We consider the signal to be validated when the likelihood of a planet exceeds that of a false positive by a sufficiently large ratio, typically at least 300 (i.e. 3σ).

Our tabulation of the viable scenarios resulting from blends was accomplished with the BLENDER algorithm (Torres et al. 2004, 2011; Fressin et al. 2011a,b) combined with some of the follow-up observations described earlier (high-resolution imaging, centroid motion analysis, spectroscopy, and *Spitzer* observations). BLENDER attempts to fit the *Kepler* photometry with a vast array of synthetic light curves generated from blend configurations consisting of chance alignments with background or foreground eclipsing binaries (EBs), as well as eclipsing binaries physically associated with Kepler-20 (hierarchical triples). We also considered cases in which the second star is eclipsed by a larger planet, rather than by another star. A wide range of parameters is explored for the eclipsing pair, as well as for the relative distance separating it from the target. Scenarios giving poor fits to the data (specifically, a χ^2 value that indicates a discrepancy of at least 3σ worse than that corresponding to the transiting planet model) are considered to be ruled out. For full details of this technique we refer the reader to the above sources.

The combination of the shorter periods and deeper transits for Kepler-20b and Kepler-20c results in higher SNR for those signals compared to the others. Consequently the shape of the transit is better defined, and this information makes it easier to reject false positives with BLENDER, as we show below. The transit depths of K00070.04 and K00070.05 are only 82 and 101 parts per million; this renders these signals far more challenging to validate, and we find below that we are currently not able to demonstrate unambiguously that these two signals are planetary in origin. Kepler-20d is similar in depth to Kepler-20b, but due to its longer orbital period, far fewer transits have been observed. This results in a lower SNR in the phase light curve. We begin by describing this case.

Figure 9 illustrates the BLENDER results for Kepler-20d. The three panels represent

cuts through the space of parameters for blends consisting of background EBs, background or foreground stars transited by larger planets, and physically associated triples. In the latter case we find that the only scenarios able to mimic the signal are those in which the companion star is orbited by a larger planet, rather than another star. The orange-red-brown-black shaded regions correspond to different levels of the χ^2 difference between blend models and the best transiting planet fit to the *Kepler* data, expressed in terms of the statistical significance of the difference (σ). The 3σ level is represented by the white contour, and only blends inside it ($< 3\sigma$) are considered to give acceptable fits to the *Kepler* photometry. Other constraints further restrict the area allowed for blends. The green hatched areas are excluded because the EB is within one magnitude of the target in the *Kp* band, and would generally have been noticed in our spectroscopic observations. The blue hatched areas are also excluded because the overall color of the blend is either too red (left in the top two panels) or too blue (right) compared to the measured Sloan-2MASS $r - K_s$ color of Kepler-20, as listed in the *Kepler* Input Catalog (KIC; Brown et al. 2011). Additionally, *Spitzer* observations rule out blends involving EBs (or star+planet pairs) with stars less massive than about $0.78 M_\odot$ (gray shaded area to the left of the vertical dotted line), because the predicted depth of the transits in the $4.5\mu\text{m}$ bandpass of Warm *Spitzer* would be more than 3σ larger than our *Spitzer* observations indicate. Note that the combination of these constraints rules out *all* physically associated triple configurations for Kepler-20d, so that only certain blend scenarios involving background EBs or background/foreground stars transited by larger planets present suitable alternatives to a true planet model.

We estimate the frequency of these remaining blends following Torres et al. (2011) and Fressin et al. (2011a), as the product of three factors: the expected number density of stars in the vicinity of Kepler-20, the area around the target within which we would miss such stars, and an estimate of how often we expect those stars to be in EBs or be transited by a larger planet of the right characteristics (specified by the stellar masses, planetary sizes, orbital eccentricities, and other characteristics as tabulated by BLENDER). For the number densities we appeal to the Besançon Galactic structure model of Robin et al. (2003). Constraints from our high-resolution imaging (see §3.1.1) allow us to estimate the maximum angular separation (ρ_{max}) at which blended stars would be undetected, as a function of brightness. We derive our estimates of the frequencies of EBs and larger transiting planets involved in blends from recent studies by the *Kepler* Team (Slawson et al. 2011; Borucki et al. 2011), in the same way as done for our earlier studies of Kepler-9 d, Kepler-10 c, and Kepler-11 g (see Torres et al. 2011; Fressin et al. 2011a; Lissauer et al. 2011b).

The results of our calculations for Kepler-20d, performed in half-magnitude bins, are shown in Table 6 separately for background EBs and for background or foreground stars transited by a larger planet. The first two columns give the *Kp* magnitude range of each bin,

and the magnitude difference ΔKp relative to the target, calculated at the faint end of each bin. Column 3 reports the stellar density near the target, subject to the mass constraints from **BLENDER** as shown in Figure 9. Column 4 gives the maximum angular separation at which background stars would escape detection in our imaging observations. In this particular case those observations are more constraining than the 3σ exclusion limit set by our analysis of the flux centroids ($0''.65$; see §3.1.1). The product of the area implied by ρ_{\max} and the densities in the previous column are listed in column 5, in units of 10^{-6} . Column 6 is the result of multiplying this number of stars by the frequency of suitable EBs ($f_{\text{EB}} = 0.78\%$; see Fressin et al. 2011a). A similar calculation is performed for blends involving stars transited by larger planets, and is presented in columns 7–10, using $f_{\text{planet}} = 0.18\%$. The latter is the frequency of planets in the radius range allowed by **BLENDER** for these types of scenarios, which is $0.4\text{--}2.0 R_{\text{Jup}}$ (see Borucki et al. 2011). The sum of the contributions in each bin is given at the bottom of columns 6 and 10. The total number of blends (i.e., the blend frequency) we expect *a priori* is reported in the last line of the table by adding these two numbers together, and is approximately $\text{BF} = 6.0 \times 10^{-7}$.

We now compare this estimate with the likelihood that Kepler-20d is a true transiting planet (planet prior). To calculate the planet prior we again make use of the census of 1,235 candidates reported by Borucki et al. (2011) among the 156,453 *Kepler* targets observed during the first four months of operation of the Mission². We count 100 candidates that are within 3σ of the measured radius ratio of Kepler-20d, implying an *a priori* transiting planet frequency of $\text{PF} = 100/156,453 = 6.4 \times 10^{-4}$. The likelihood of a planet is therefore several orders of magnitude larger than the likelihood of a false positive ($\text{PF}/\text{BF} = 6.4 \times 10^{-4}/6.0 \times 10^{-7} \approx 1100$), and we consider Kepler-20d to be validated as a planet with a high degree of confidence.

The transit signals from Kepler-20b and Kepler-20c are better defined, and as a result **BLENDER** is able to rule out all scenarios involving background EBs consisting of two stars, as well as all physically associated triples. This reduces the blend frequencies by one to two orders of magnitude compared to Kepler-20d. For Kepler-20c, *Spitzer* observations are available as well, although the constraints they provide are redundant with color information also available for the star, which already rules out contaminants of late spectral type. The areas of parameter space in which **BLENDER** finds false positives providing acceptable fits to the photometry are shown in Figure 10. The detailed calculations of the blend frequencies for

²While these 1,235 candidates have not yet been confirmed as true planets, the rate of false positives is expected to be quite low (10% or less; see Morton & Johnson 2011), so our results will not be significantly affected by the assumption that all of the candidates are planets. We further assume here that the census of Borucki et al. (2011) is complete at these planetary radii.

Kepler-20b and Kepler-20c are presented in Table 7 and Table 8, respectively, using appropriate ranges for the larger planets orbiting the blended stars as allowed by BLENDER, along with the corresponding transiting planet frequencies specified in the headings of column 6.

Planet priors for these two candidates were computed as before using the catalog of Borucki et al. (2011). We count 52 cases in that list within 3σ of the measured radius ratio of Kepler-20b, leading to an *a priori* planet frequency of $52/156,453 = 3.3 \times 10^{-4}$. This is nearly 20,000 times larger than the blend frequency given in Table 7 ($\text{BF} = 1.7 \times 10^{-8}$). For Kepler-20c the planet prior based on the measured radius ratio is $28/156,453 = 1.8 \times 10^{-4}$, which is approximately 10^5 times larger than the likelihood of a blend. Therefore, both Kepler-20b and Kepler-20c are validated as planets with a very high degree of confidence.

We carried out similar calculations for the candidates K00070.04 and K00070.05. The transit signals of these two candidates are much more shallow than those of Kepler-20b, Kepler-20c, and Kepler-20d. As a result, the constraint on the shape of the transit is considerably weaker than in the cases described above, and many more false positives than before are found with BLENDER that provide acceptable fits within 3σ of the quality of a planet model. Additionally, neither of these candidates were observed with *Spitzer*, so the constraint on the near-infrared depth of the transit that allowed us to rule out some of the blends for Kepler-20d is not available here. In particular, physically associated stars transited by a larger planet cannot all be ruled out, and this ends up contributing significantly to the overall blend frequency. We conclude that the BLENDER methodology as implemented above is insufficient to validate either K00070.04 or K00070.05, and we defer this issue to a subsequent study (Fressin et al. 2012).

Table 6. Blend frequency estimate for Kepler-20d (K00070.03).

Kp Range (mag) (1)	ΔKp (mag) (2)	Blends Involving Stellar Tertiaries				Blends Involving Planetary Tertiaries			
		Stellar Density ^a (per sq. deg) (3)	ρ_{\max} ($''$) (4)	Stars ($\times 10^{-6}$) (5)	EBs $f_{\text{EB}} = 0.78\%$ (6)	Stellar Density ^a (per sq. deg) (7)	ρ_{\max} ($''$) (8)	Stars ($\times 10^{-6}$) (9)	Blends ($\times 10^{-6}$) $R_p \in [0.4 - 2.0 R_{\text{Jup}}], f_{\text{Plan}} = 0.18\%$ (10)
12.5–13.0	0.5
13.0–13.5	1.0
13.5–14.0	1.5	28	0.075	0.038	0.0003	273	0.075	0.372	0.0007
14.0–14.5	2.0	77	0.093	0.164	0.0013	423	0.093	0.901	0.0016
14.5–15.0	2.5	119	0.11	0.349	0.0028	572	0.11	1.678	0.0024
15.0–15.5	3.0	238	0.13	0.975	0.0077	897	0.13	3.675	0.0053
15.5–16.0	3.5	532	0.15	2.902	0.0229	1183	0.15	6.452	0.0093
16.0–16.5	4.0	1321	0.20	12.81	0.1012	1675	0.20	16.24	0.0234
16.5–17.0	4.5	1593	0.25	24.13	0.1907
17.0–17.5	5.0	1295	0.30	28.25	0.2232
17.5–18.0	5.5
18.5–19.0	6.0
19.0–19.5	6.5
19.5–20.0	7.0
20.0–20.5	7.5
20.5–21.0	8.0
Totals		5203	...	69.62	0.5511	5023	...	29.32	0.0526

Blend frequency (BF) = $(0.5511 + 0.0526) \times 10^{-6} \approx 6.04 \times 10^{-7}$

^aThe number densities in Columns 3 and 7 differ because of the different secondary mass ranges permitted by BLENDER for the two kinds of blend scenarios, as shown in the top two panels of Figures 9.

Note. — Magnitude bins with no entries correspond to brightness ranges in which all blends are ruled out by a combination of BLENDER and other constraints.

Table 7. Blend frequency estimate for Kepler-20b (K00070.02).

Blends Involving Planetary Tertiaries					
Kp Range (mag) (1)	ΔKp (mag) (2)	Stellar Density (per sq. deg) (3)	ρ_{\max} ($''$) (4)	Stars ($\times 10^{-6}$) (5)	Blends ($\times 10^{-6}$) $R_p \in [0.27 - 1.81 R_{\text{Jup}}]$, $f_{\text{Plan}} = 0.29\%$ (6)
12.5–13.0	0.5
13.0–13.5	1.0
13.5–14.0	1.5	271	0.075	0.370	0.00068
14.0–14.5	2.0	379	0.093	0.807	0.00149
14.5–15.0	2.5	404	0.11	1.185	0.00218
15.0–15.5	3.0	464	0.13	1.901	0.00351
15.5–16.0	3.5	498	0.15	2.716	0.00501
16.0–16.5	4.0	255	0.20	2.473	0.00456
16.5–17.0	4.5
17.0–17.5	5.0
17.5–18.0	5.5
18.0–18.5	6.0
18.5–19.0	6.5
19.0–19.5	7.0
19.5–20.0	7.5
20.0–20.5	8.0
Totals		2669	...	9.452	0.0174

Blend frequency (BF) = 1.74×10^{-8}

Note. — Magnitude bins with no entries correspond to brightness ranges in which all blends are ruled out by a combination of BLENDER and other constraints.

Table 8. Blend frequency estimate for Kepler-20c (K00070.01).

Blends Involving Planetary Tertiaries					
Kp Range (mag) (1)	ΔKp (mag) (2)	Stellar Density (per sq. deg) (3)	ρ_{\max} ($''$) (4)	Stars ($\times 10^{-6}$) (5)	Blends ($\times 10^{-6}$) $R_p \in [0.39 - 1.95 R_{\text{Jup}}]$, $f_{\text{Plan}} = 0.18\%$ (6)
12.5–13.0	0.5
13.0–13.5	1.0
13.5–14.0	1.5	221	0.075	0.300	0.00056
14.0–14.5	2.0	274	0.093	0.551	0.00108
14.5–15.0	2.5
15.0–15.5	3.0
15.5–16.0	3.5
16.0–16.5	4.0
16.5–17.0	4.5
17.0–17.5	5.0
17.5–18.0	5.5
18.0–18.5	6.0
18.5–19.0	6.5
19.0–19.5	7.0
19.5–20.0	7.5
Totals		495	...	0.851	0.00164
Blend frequency (BF) = 1.64×10^{-9}					

Note. — Magnitude bins with no entries correspond to brightness ranges in which all blends are ruled out by a combination of BLENDER and other constraints.

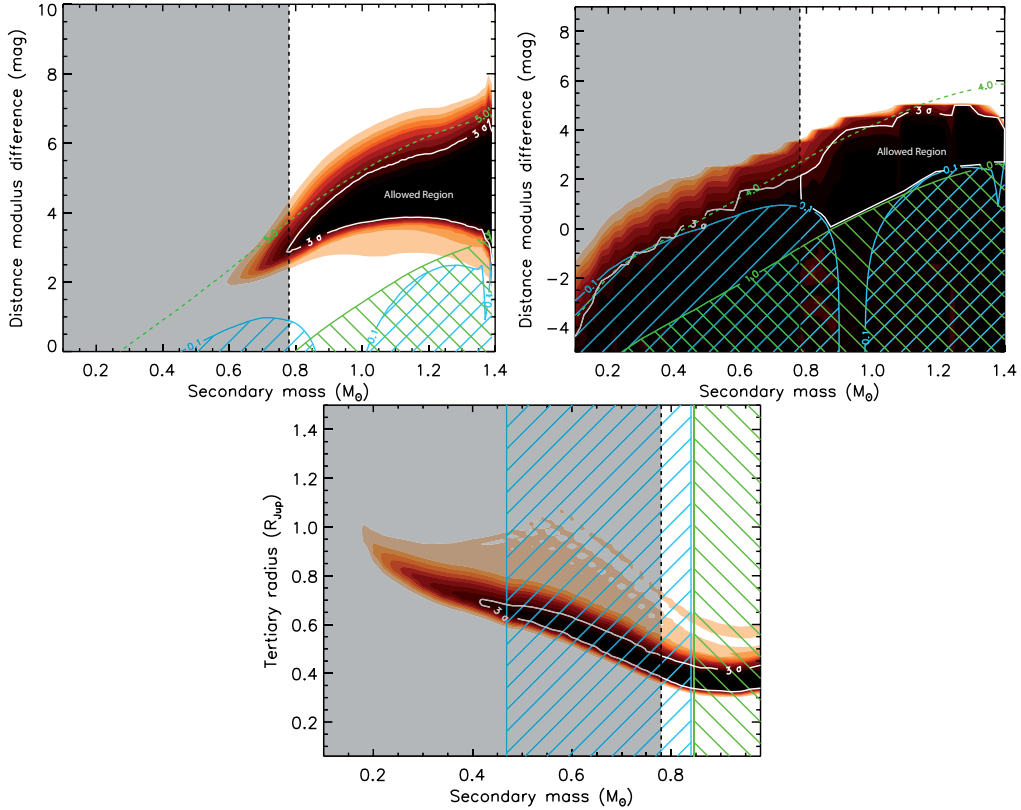


Fig. 9.— BLENDER goodness-of-fit contours corresponding to three different blend scenarios for Kepler-20d: background EBs (*top left*), background or foreground stars transited by a larger planet (*top right*), and stars physically associated with the target that are transited by a larger planet (*bottom*). The mass of the intruding star (referred to in the BLENDER nomenclature as the secondary) is shown along the horizontal axis, and the distance between this star and the target is shown on the vertical axis of the top two panels, expressed for convenience in terms of the distance modulus difference. The vertical axis in the bottom panel shows the sizes of the planets (tertiaries) orbiting physically associated stars. Viable blend models are those giving fits with χ^2 values within 3σ of the best planet fit, and lie inside the white contours. Other colored areas outside the white contours indicate regions of parameter space with increasingly worse fits to the data. Blends excluded by our *Spitzer* constraints are shown with the shaded gray area (secondary masses $< 0.78 M_{\odot}$). Blue cross-hatched areas indicate regions in which blends are excluded because they are either too red (left) or too blue (right) compared to the measured $r - K_s$ color of Kepler-20. Blend scenarios in the green cross-hatched areas are also ruled out because they are within $\Delta Kp = 1.0$ of the brightness of the target, and would have been detected spectroscopically. The dashed diagonal green lines in the top panels mark the faintest blends that give acceptable fits to the light curve, corresponding to $\Delta Kp \approx 5$ in the top left panel and $\Delta Kp \approx 4$ in the top right panel. As a result of the combined constraints from our *Spitzer* observations, color index, and brightness, *all* physically associated triples are excluded.

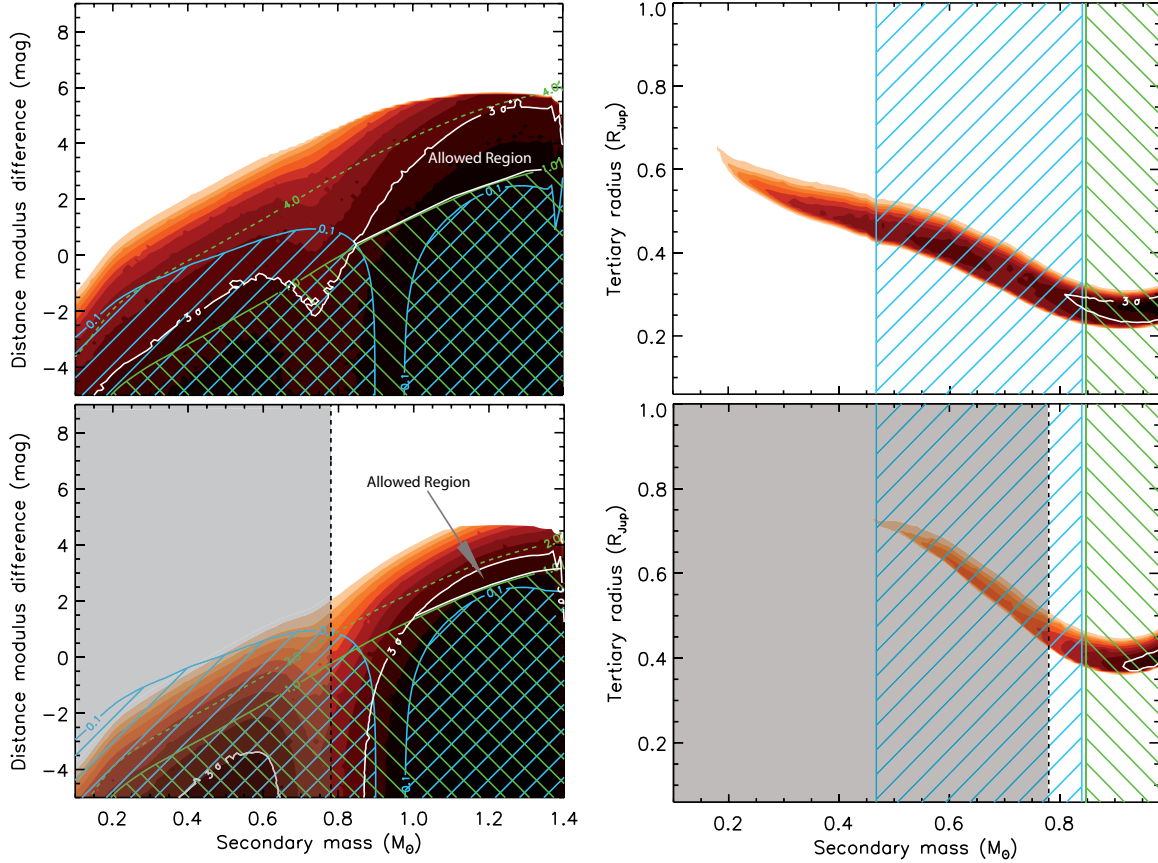


Fig. 10.— BLENDER constraints for Kepler-20b (*top panels*) and Kepler-20c (*bottom*), showing chance alignments with a star+planet pair on the left and physically associated stellar companions transited by a larger planet on the right. See Figure 9 for the meaning of the various lines. The space of parameters for background EBs is not shown as all of those scenarios provide very poor fits to the transit light curve, and are ruled out. All blends involving physically associated stars transited by a larger planet (*right panels*) are excluded by a combination of spectroscopic constraints (specifically, on the absence of a secondary spectrum) and color constraints.

5. Constraints on Transit Times and Long-term Stability

In this section we discuss the transit times and long-term stability of the system of planets orbiting Kepler-20. Both are consistent with the planet interpretation for all 5 candidates: transit timing variations (TTVs; Holman & Murray 2005; Agol et al. 2005) are not seen or expected, and the system is expected to be stable over long timescales.

The individual transit times are measured by allowing a template transit light curve to slide in time to fit the data for each transit (Ford et al. 2011). The resulting transit times are given in Table 9. Aside from slightly more scatter than expected from the formal error bars there is no indication of perturbations such as coherent patterns. Such excess scatter is not atypical of transit times measured by the standard pipeline (Ford et al. 2011). Thus, we find no evidence for dynamical interactions among either the transiting planets or additional, non-transiting planets.

To calculate predicted transit times, we numerically integrate our baseline model, which consists of a central star of mass $0.912 M_{\odot}$ surrounded by planets with periods and epochs given in Table 2 (given at dynamical epoch BJD 2454170), and with masses of 8.7, 0.65, 16.1, 1.1 and $8.0 M_{\oplus}$ (from least to greatest orbital period), corresponding to the best-fit masses for Kepler-20b and Kepler-20c, a guess of $M_p = M_{\oplus} (R_p/R_{\oplus})^{2.06}$ (Lissauer et al. 2011b) for Kepler-20d, and masses giving Earth’s density for K00070.04 and K00070.05. (We remind the reader that we have not, in this paper, validated these two candidates as planets. However, considering them as such for the purposes of evaluating dynamical stability is the conservative choice, since the presence of 5 planets, as opposed to 3, is more likely to induce dynamical instabilities. Fressin et al. (2012) presents the validation of K00070.04 and K00070.05, gives their sizes, from which the masses above are derived, and discusses constraints on their masses.) The orbits are chosen to be initially circular, coplanar, and edge-on to the line of sight. The root mean square deviations of the model transit times from the best-fit linear ephemeris projected over 8 years are approximately 3s, 76s, 9s, 95s and 10s (from least to greatest orbital period), all significantly smaller than the measurement precision shown in Figure 11.

Next, we investigated long-term stability for this system by integrating the baseline model with the hybrid algorithm in Mercury (Chambers 1999). As no close encounters were recorded, this algorithm reduced to the symplectic algorithm (Wisdom & Holman 1991), with time steps of 0.1 days, roughly 2.7% of the period of the innermost planet. Over the 10 Myr integration duration, there were no indications of instability. The orbital eccentricities fluctuated on the scale between approximately 3×10^{-5} (for Kepler-20d) and 0.001 (for K00070.04). We conclude that plausible, low-eccentricity models for the system are stable over long timescales.

Finally, we performed an ensemble of N-body integrations using the time-symmetric 4th order Hermite integrator (Kokubo et al. 1998) implemented in **Swarm-NG**³ to estimate the maximum plausible eccentricity for each planet consistent with long-term stability. For each N-body integration, we set four planets on circular orbits and assigned one planet a non-zero eccentricity. The eccentricity and pericenter directions for the planet on a non-circular orbit were drawn from uniform distributions. The maximum for the uniform distribution of eccentricities was chosen to be slightly larger than necessary for its orbit to cross one of its neighbors. We report e_{\max} , the maximum initial eccentricity that resulted in a system with no close encounters (within one mutual Hill radius) and semi-major axes (in a Jacobi frame) which varied by less than 1% for the duration of the integrations. Based on 100 integrations per planet and relatively short integrations (10^5 years), we estimate e_{\max} to be 0.19, 0.16, 0.16, 0.38 and 0.55 (from smallest to largest orbital period). Technically, we can not completely exclude larger eccentricities, due to various assumptions (such as the planet masses, coplanarity, prograde orbits, absence of false positives, and the potential for small islands of stability at higher eccentricity). Nevertheless, the N-body integrations support the assumption of non-crossing orbits, as the vast majority of systems with an eccentricity larger than e_{\max} are dynamical unstable.

³www.astro.ufl.edu/~eford/code/swarm/

Table 9. Transit Times for Kepler-20 *We request that this table be published in electronic format.*

ID	n	t_n BJD-2454900	TTV _n (d)	σ_n (d)
Kepler-20b		$67.50027 + n \times 3.6961219$		
Kepler-20b	0	67.4942	-0.0061	0.0032
Kepler-20b	1	71.1956	-0.0008	0.0035
Kepler-20b	2	74.8946	0.0021	0.0041
Kepler-20b	3	78.5836	-0.0050	0.0035
Kepler-20b	4	82.2857	0.0009	0.0034
Kepler-20b	5	85.9768	-0.0040	0.0032
Kepler-20b	6	89.6783	0.0013	0.0045
Kepler-20b	7	93.3689	-0.0042	0.0037
Kepler-20b	8	97.0699	0.0007	0.0071
Kepler-20b	10	104.4602	-0.0012	0.0039
Kepler-20b	11	108.1582	0.0006	0.0028
Kepler-20b	12	111.8565	0.0028	0.0049
Kepler-20b	14	119.2447	-0.0013	0.0036
Kepler-20b	15	122.9460	0.0039	0.0043
Kepler-20b	16	126.6347	-0.0035	0.0044
Kepler-20b	17	130.3393	0.0050	0.0034
Kepler-20b	18	134.0237	-0.0068	0.0034
Kepler-20b	19	137.7315	0.0049	0.0044
Kepler-20b	20	141.4302	0.0075	0.0043
Kepler-20b	21	145.1190	0.0001	0.0027
Kepler-20b	22	148.8142	-0.0007	0.0034
Kepler-20b	23	152.5058	-0.0052	0.0031
Kepler-20b	24	156.2050	-0.0022	0.0034
Kepler-20b	25	159.8994	-0.0039	0.0045
Kepler-20b	27	167.2983	0.0027	0.0035
Kepler-20b	28	170.9908	-0.0009	0.0036
Kepler-20b	29	174.6887	0.0009	0.0078
Kepler-20b	30	178.3859	0.0020	0.0028
Kepler-20b	31	182.0814	0.0013	0.0038
Kepler-20b	32	185.7734	-0.0027	0.0038
Kepler-20b	33	189.4547	-0.0176	0.0103
Kepler-20b	35	196.8662	0.0016	0.0038
Kepler-20b	36	200.5665	0.0059	0.0036
Kepler-20b	37	204.2595	0.0027	0.0026
Kepler-20b	38	207.9564	0.0035	0.0032
Kepler-20b	39	211.6447	-0.0043	0.0030
Kepler-20b	40	215.3402	-0.0049	0.0054
Kepler-20b	41	219.0422	0.0009	0.0040
Kepler-20b	42	222.7391	0.0017	0.0048
Kepler-20b	43	226.4399	0.0064	0.0052
Kepler-20b	44	230.1275	-0.0022	0.0024
Kepler-20b	45	233.8232	-0.0025	0.0031
Kepler-20b	46	237.5259	0.0041	0.0043
Kepler-20b	47	241.2178	-0.0002	0.0037

Table 9—Continued

ID	n	t_n BJD-2454900	TTV _n (d)	σ_n (d)
Kepler-20b	48	244.9212	0.0071	0.0035
Kepler-20b	49	248.6075	-0.0028	0.0033
Kepler-20b	50	252.3057	-0.0007	0.0045
Kepler-20b	52	259.6893	-0.0093	0.0043
Kepler-20b	53	263.4017	0.0070	0.0046
Kepler-20b	54	267.0944	0.0036	0.0039
Kepler-20b	55	270.7832	-0.0038	0.0051
Kepler-20b	56	274.4814	-0.0017	0.0042
Kepler-20b	57	278.1816	0.0024	0.0049
Kepler-20b	58	281.8728	-0.0026	0.0041
Kepler-20b	59	285.5734	0.0020	0.0044
Kepler-20b	60	289.2635	-0.0041	0.0041
Kepler-20b	61	292.9654	0.0017	0.0053
Kepler-20b	62	296.6559	-0.0040	0.0028
Kepler-20b	63	300.3544	-0.0015	0.0039
Kepler-20b	64	304.0540	0.0019	0.0035
Kepler-20b	65	307.7479	-0.0002	0.0040
Kepler-20b	66	311.4449	0.0005	0.0045
Kepler-20b	67	315.1474	0.0070	0.0042
Kepler-20b	68	318.8345	-0.0020	0.0045
Kepler-20b	69	322.5374	0.0048	0.0040
Kepler-20b	70	326.2274	-0.0014	0.0039
Kepler-20b	74	341.0195	0.0062	0.0040
Kepler-20b	75	344.7166	0.0072	0.0041
Kepler-20b	76	348.4024	-0.0031	0.0048
Kepler-20b	77	352.1038	0.0022	0.0038
Kepler-20b	78	355.8025	0.0047	0.0029
Kepler-20b	79	359.4904	-0.0035	0.0043
Kepler-20b	80	363.1916	0.0016	0.0045
Kepler-20b	81	366.8831	-0.0031	0.0041
Kepler-20b	82	370.5829	0.0006	0.0037
Kepler-20b	83	374.2740	-0.0044	0.0027
Kepler-20b	84	377.9727	-0.0018	0.0040
Kepler-20b	85	381.6793	0.0086	0.0039
Kepler-20b	86	385.3678	0.0011	0.0033
Kepler-20b	87	389.0654	0.0025	0.0041
Kepler-20b	88	392.7595	0.0005	0.0045
Kepler-20b	89	396.4618	0.0067	0.0042
Kepler-20b	90	400.1460	-0.0053	0.0042
Kepler-20b	91	403.8471	-0.0003	0.0043
Kepler-20b	92	407.5457	0.0022	0.0027
Kepler-20b	93	411.2340	-0.0056	0.0049
Kepler-20b	94	414.9291	-0.0066	0.0036
Kepler-20b	95	418.6325	0.0007	0.0034
Kepler-20b	96	422.3282	0.0003	0.0029

Table 9—Continued

ID	n	t_n BJD-2454900	TTV $_n$ (d)	σ_n (d)
Kepler-20b	97	426.0243	0.0002	0.0017
Kepler-20b	98	429.7166	-0.0036	0.0043
Kepler-20b	99	433.4211	0.0047	0.0030
Kepler-20b	101	440.8062	-0.0024	0.0049
Kepler-20b	102	444.4994	-0.0053	0.0044
Kepler-20b	103	448.2026	0.0018	0.0035
Kepler-20b	104	451.9098	0.0129	0.0053
Kepler-20b	105	455.5917	-0.0013	0.0045
Kepler-20b	106	459.2855	-0.0037	0.0039
Kepler-20b	107	462.9828	-0.0025	0.0027
Kepler-20b	108	466.6899	0.0084	0.0038
Kepler-20b	109	470.3763	-0.0012	0.0040
Kepler-20b	110	474.0741	0.0004	0.0041
Kepler-20b	111	477.7694	-0.0004	0.0033
Kepler-20b	112	481.4629	-0.0030	0.0034
Kepler-20b	113	485.1567	-0.0053	0.0034
Kepler-20b	114	488.8559	-0.0023	0.0025
Kepler-20b	115	492.5534	-0.0009	0.0035
Kepler-20b	116	496.2526	0.0022	0.0033
Kepler-20b	118	503.6411	-0.0015	0.0039
Kepler-20b	119	507.3215	-0.0173	0.0045
Kepler-20b	120	511.0371	0.0022	0.0055
Kepler-20b	121	514.7318	0.0008	0.0049
Kepler-20b	122	518.4255	-0.0016	0.0027
Kepler-20b	123	522.1195	-0.0037	0.0043
Kepler-20b	124	525.8160	-0.0034	0.0030
Kepler-20b	125	529.5154	-0.0001	0.0044
Kepler-20b	126	533.2147	0.0031	0.0046
Kepler-20b	127	536.9038	-0.0039	0.0029
Kepler-20b	128	540.6034	-0.0004	0.0037
Kepler-20b	129	544.3084	0.0084	0.0042
Kepler-20b	130	548.0018	0.0057	0.0041
Kepler-20b	131	551.6946	0.0024	0.0035
Kepler-20b	132	555.3912	0.0028	0.0030
Kepler-20b	133	559.0861	0.0016	0.0037
Kepler-20b	135	566.4817	0.0050	0.0043
Kepler-20b	136	570.1738	0.0009	0.0054
Kepler-20b	137	573.8736	0.0046	0.0032
Kepler-20b	138	577.5612	-0.0039	0.0040
Kepler-20b	139	581.2539	-0.0074	0.0051
Kepler-20b	140	584.9482	-0.0092	0.0040
Kepler-20b	141	588.6502	-0.0032	0.0035
Kepler-20b	142	592.3510	0.0014	0.0050
Kepler-20b	143	596.0490	0.0033	0.0034
Kepler-20b	144	599.7493	0.0075	0.0044

Table 9—Continued

ID	n	t_n BJD-2454900	TTV $_n$ (d)	σ_n (d)
Kepler-20b	145	603.4392	0.0013	0.0056
Kepler-20b	146	607.1344	0.0004	0.0038
Kepler-20b	147	610.8329	0.0027	0.0043
Kepler-20b	148	614.5286	0.0023	0.0032
Kepler-20b	149	618.2205	-0.0019	0.0027
Kepler-20b	150	621.9156	-0.0029	0.0031
Kepler-20b	151	625.6180	0.0033	0.0039
Kepler-20b	152	629.3115	0.0007	0.0039
Kepler-20b	153	633.0118	0.0049	0.0050
Kepler-20b	154	636.6958	-0.0072	0.0043
Kepler-20b	155	640.3937	-0.0054	0.0045
Kepler-20b	157	647.7922	0.0008	0.0046
Kepler-20b	158	651.4935	0.0060	0.0042
Kepler-20b	163	669.9606	-0.0075	0.0041
Kepler-20b	164	673.6626	-0.0017	0.0094
Kepler-20b	165	677.3552	-0.0052	0.0037
Kepler-20b	166	681.0550	-0.0015	0.0062
Kepler-20b	167	684.7541	0.0014	0.0030
Kepler-20b	168	688.4526	0.0038	0.0046
Kepler-20b	169	692.1463	0.0014	0.0017
Kepler-20b	171	699.5324	-0.0047	0.0039
Kepler-20b	172	703.2330	-0.0002	0.0067
Kepler-20b	173	706.9307	0.0014	0.0038
Kepler-20b	174	710.6210	-0.0045	0.0032
Kepler-20b	175	714.3175	-0.0041	0.0037
Kepler-20b	176	718.0073	-0.0105	0.0063
Kepler-20b	177	721.7094	-0.0044	0.0042
Kepler-20b	178	725.4097	-0.0003	0.0039
Kepler-20b	179	729.1068	0.0007	0.0039
Kepler-20b	180	732.8057	0.0035	0.0032
70.04		$68.9336 + n \times 6.098493$		
70.04	0	68.9295	-0.0041	0.0124
70.04	1	75.0316	-0.0005	0.0149
70.04	2	81.1487	0.0181	0.0116
70.04	3	87.1926	-0.0364	0.0176
70.04	4	93.2997	-0.0278	0.0117
70.04	6	105.5245	-0.0001	0.0103
70.04	7	111.6445	0.0215	0.0150
70.04	8	117.6964	-0.0251	0.0150
70.04	9	123.8323	0.0123	0.0138
70.04	10	129.9095	-0.0090	0.0122
70.04	11	135.9953	-0.0217	0.0525
70.04	12	142.0980	-0.0175	0.0176
70.04	13	148.2067	-0.0073	0.0211
70.04	14	154.3205	0.0080	0.0156

Table 9—Continued

ID	n	t_n BJD-2454900	TTV $_n$ (d)	σ_n (d)
70.04	15	160.4350	0.0240	0.0122
70.04	16	166.5186	0.0091	0.0152
70.04	17	172.6143	0.0063	0.0123
70.04	18	178.7111	0.0047	0.0141
70.04	19	184.8108	0.0059	0.0503
70.04	20	190.9342	0.0307	0.0171
70.04	21	196.9966	-0.0054	0.0137
70.04	22	203.1011	0.0007	0.0148
70.04	23	209.2095	0.0106	0.0177
70.04	24	215.3090	0.0115	0.0181
70.04	25	221.3969	0.0010	0.0163
70.04	26	227.5457	0.0513	0.0112
70.04	27	233.6113	0.0183	0.0132
70.04	28	239.7084	0.0170	0.0226
70.04	29	245.7739	-0.0160	0.0192
70.04	30	251.8802	-0.0082	0.0147
70.04	31	257.9671	-0.0198	0.0147
70.04	32	264.0366	-0.0488	0.0175
70.04	33	270.1797	-0.0042	0.0314
70.04	34	276.2872	0.0048	0.0161
70.04	35	282.3650	-0.0159	0.0197
70.04	36	288.4550	-0.0244	0.0211
70.04	37	294.5290	-0.0489	0.0186
70.04	38	300.6801	0.0037	0.0163
70.04	39	306.7537	-0.0211	0.0169
70.04	40	312.9025	0.0292	0.0190
70.04	41	318.9743	0.0024	0.0131
70.04	42	325.0517	-0.0186	0.0129
70.04	45	343.4285	0.0627	0.0183
70.04	46	349.4757	0.0114	0.0189
70.04	47	355.5391	-0.0236	0.0120
70.04	48	361.6421	-0.0192	0.0113
70.04	49	367.7477	-0.0120	0.0104
70.04	50	373.8366	-0.0217	0.0106
70.04	51	379.9503	-0.0065	0.0109
70.04	52	386.0611	0.0059	0.0128
70.04	53	392.1451	-0.0086	0.0139
70.04	54	398.2748	0.0226	0.0204
70.04	55	404.3426	-0.0082	0.0139
70.04	57	416.5261	-0.0216	0.0164
70.04	58	422.6521	0.0059	0.0142
70.04	59	428.7752	0.0305	0.0155
70.04	60	434.8565	0.0133	0.0164
70.04	61	440.9316	-0.0101	0.0151
70.04	62	447.0528	0.0127	0.0172

Table 9—Continued

ID	n	t_n BJD-2454900	TTV $_n$ (d)	σ_n (d)
70.04	63	453.1351	-0.0035	0.0135
70.04	64	459.2399	0.0028	0.0119
70.04	65	465.3240	-0.0116	0.0147
70.04	67	477.5344	0.0017	0.0120
70.04	68	483.6637	0.0326	0.0097
70.04	69	489.7101	-0.0195	0.0152
70.04	70	495.8219	-0.0062	0.0158
70.04	71	501.9295	0.0029	0.0135
70.04	72	507.9607	-0.0644	0.0155
70.04	73	514.1161	-0.0075	0.0148
70.04	74	520.1992	-0.0229	0.0127
70.04	75	526.3201	-0.0005	0.0121
70.04	76	532.4389	0.0198	0.0133
70.04	77	538.5127	-0.0049	0.0143
70.04	78	544.6282	0.0121	0.0113
70.04	79	550.7134	-0.0011	0.0182
70.04	80	556.8084	-0.0046	0.0092
70.04	82	568.9873	-0.0227	0.0189
70.04	83	575.1346	0.0261	0.0154
70.04	84	581.2328	0.0258	0.0157
70.04	85	587.2972	-0.0083	0.0147
70.04	87	599.4992	-0.0033	0.0139
70.04	88	605.6078	0.0068	0.0158
70.04	89	611.6560	-0.0435	0.0111
70.04	90	617.8120	0.0141	0.0169
70.04	92	630.0025	0.0075	0.0151
70.04	93	636.1181	0.0247	0.0147
70.04	94	642.1929	0.0010	0.0106
70.04	95	648.3022	0.0118	0.0171
70.04	99	672.6873	0.0029	0.0192
70.04	100	678.7764	-0.0065	0.0153
70.04	101	684.8819	0.0006	0.0144
70.04	102	690.9771	-0.0027	0.0165
70.04	103	697.0837	0.0053	0.0166
70.04	104	703.1848	0.0079	0.0228
70.04	105	709.3466	0.0713	0.0171
70.04	106	715.3852	0.0113	0.0108
70.04	107	721.4592	-0.0132	0.0155
70.04	108	727.5689	-0.0019	0.0169
70.04	109	733.6590	-0.0104	0.0103
Kepler-20c		$71.6076 + n \times 10.85409$		
Kepler-20c	0	71.6063	-0.0013	0.0018
Kepler-20c	1	82.4610	-0.0007	0.0027
Kepler-20c	2	93.3240	0.0083	0.0033
Kepler-20c	3	104.1716	0.0017	0.0024

Table 9—Continued

ID	n	t_n BJD-2454900	TTV _n (d)	σ_n (d)
Kepler-20c	5	125.8775	-0.0005	0.0020
Kepler-20c	6	136.7324	0.0003	0.0018
Kepler-20c	7	147.5848	-0.0014	0.0018
Kepler-20c	8	158.4418	0.0015	0.0013
Kepler-20c	9	169.2901	-0.0043	0.0014
Kepler-20c	10	180.1483	-0.0002	0.0018
Kepler-20c	11	191.0000	-0.0025	0.0018
Kepler-20c	12	201.8560	-0.0006	0.0015
Kepler-20c	13	212.7127	0.0020	0.0016
Kepler-20c	14	223.5737	0.0089	0.0034
Kepler-20c	15	234.4203	0.0014	0.0023
Kepler-20c	16	245.2744	0.0013	0.0013
Kepler-20c	18	266.9898	0.0086	0.0027
Kepler-20c	19	277.8388	0.0034	0.0018
Kepler-20c	20	288.6911	0.0017	0.0019
Kepler-20c	21	299.5445	0.0009	0.0018
Kepler-20c	22	310.3963	-0.0013	0.0016
Kepler-20c	23	321.2501	-0.0016	0.0018
Kepler-20c	25	342.9608	0.0009	0.0018
Kepler-20c	26	353.8129	-0.0011	0.0014
Kepler-20c	27	364.6678	-0.0003	0.0014
Kepler-20c	29	386.3751	-0.0011	0.0020
Kepler-20c	30	397.2301	-0.0002	0.0013
Kepler-20c	32	418.9392	0.0007	0.0021
Kepler-20c	33	429.7823	-0.0103	0.0032
Kepler-20c	34	440.6474	0.0007	0.0032
Kepler-20c	35	451.5008	0.0000	0.0012
Kepler-20c	36	462.3549	0.0000	0.0022
Kepler-20c	37	473.2071	-0.0019	0.0015
Kepler-20c	38	484.0631	0.0000	0.0017
Kepler-20c	39	494.9177	0.0006	0.0029
Kepler-20c	40	505.7737	0.0024	0.0011
Kepler-20c	41	516.6244	-0.0010	0.0016
Kepler-20c	42	527.4780	-0.0015	0.0013
Kepler-20c	43	538.3328	-0.0008	0.0014
Kepler-20c	44	549.1875	-0.0001	0.0021
Kepler-20c	45	560.0406	-0.0011	0.0015
Kepler-20c	46	570.8982	0.0024	0.0014
Kepler-20c	47	581.7495	-0.0004	0.0021
Kepler-20c	48	592.6034	-0.0006	0.0034
Kepler-20c	49	603.4558	-0.0023	0.0033
Kepler-20c	50	614.3101	-0.0021	0.0023
Kepler-20c	51	625.1658	-0.0005	0.0014
Kepler-20c	52	636.0218	0.0014	0.0014
Kepler-20c	53	646.8745	0.0000	0.0016

Table 9—Continued

ID	n	t_n BJD-2454900	TTV $_n$ (d)	σ_n (d)
Kepler-20c	55	668.5835	0.0009	0.0016
Kepler-20c	56	679.4363	-0.0005	0.0025
Kepler-20c	57	690.2898	-0.0010	0.0023
Kepler-20c	58	701.1466	0.0017	0.0023
Kepler-20c	59	711.9975	-0.0015	0.0018
Kepler-20c	60	722.8602	0.0071	0.0024
Kepler-20c	61	733.7038	-0.0034	0.0014
70.05		$68.219 + n \times 19.57706$		
70.05	0	68.2114	-0.0076	0.0111
70.05	1	87.7637	-0.0323	0.0155
70.05	2	107.3404	-0.0327	0.0149
70.05	3	126.9232	-0.0270	0.0161
70.05	4	146.5711	0.0439	0.0177
70.05	5	166.0304	-0.0739	0.0121
70.05	6	185.6525	-0.0289	0.0138
70.05	7	205.2436	-0.0149	0.0191
70.05	8	224.8237	-0.0117	0.0134
70.05	9	244.4134	0.0009	0.0259
70.05	10	264.0047	0.0151	0.0129
70.05	12	303.1682	0.0245	0.0134
70.05	13	322.7048	-0.0160	0.0135
70.05	14	342.2962	-0.0017	0.0119
70.05	15	361.8658	-0.0091	0.0217
70.05	16	381.4339	-0.0181	0.0154
70.05	17	401.0316	0.0025	0.0157
70.05	18	420.5948	-0.0113	0.0129
70.05	19	440.1844	0.0013	0.0128
70.05	20	459.7616	0.0014	0.0193
70.05	21	479.3348	-0.0024	0.0110
70.05	22	498.9270	0.0127	0.0138
70.05	23	518.4884	-0.0030	0.0113
70.05	24	538.0258	-0.0427	0.0118
70.05	25	557.6534	0.0079	0.0114
70.05	26	577.2165	-0.0061	0.0207
70.05	27	596.8058	0.0062	0.0157
70.05	28	616.4009	0.0242	0.0148
70.05	29	635.9785	0.0247	0.0145
70.05	31	675.1005	-0.0074	0.0192
70.05	33	714.2609	-0.0010	0.0139
70.05	34	733.8455	0.0065	0.0101
Kepler-20d		$97.7271 + n \times 77.61184$		
Kepler-20d	0	97.7293	0.0022	0.0029
Kepler-20d	1	175.3387	-0.0002	0.0022
Kepler-20d	2	252.9482	-0.0026	0.0040
Kepler-20d	5	485.7834	-0.0029	0.0022

Table 9—Continued

ID	n	t_n BJD-2454900	TTV $_n$ (d)	σ_n (d)
Kepler-20d	6	563.4005	0.0024	0.0029
Kepler-20d	7	641.0100	0.0001	0.0022
Kepler-20d	8	718.6231	0.0013	0.0026

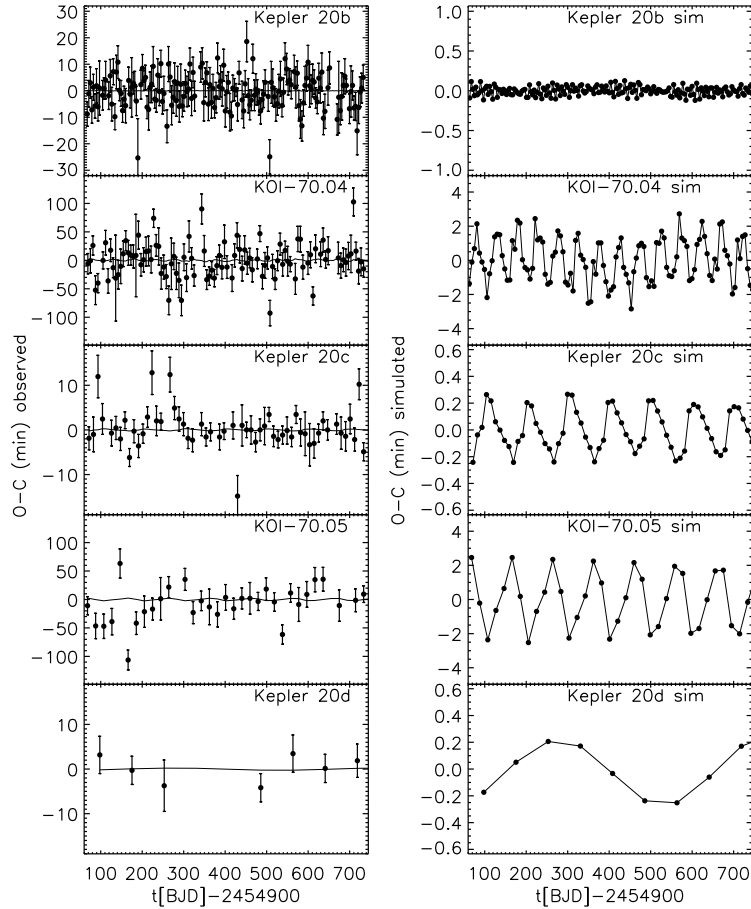


Fig. 11.— Measured and predicted transit timing for the planets of Kepler-20. *Left panels:* Observed times minus calculated times according to a constant-period model ($O - C$) are plotted as points with error bars, versus transit time. The timing simulations using circular, coplanar planets with nominal masses are plotted as lines. *Right panels:* The simulations are shown in more detail ($30\times$ zoom of each panel) to show the timescale and structure of variations.

6. Constraints on the Planetary Compositions and Formation History

The Kepler-20 system, harboring multiple sub-Neptune planets with constrained radii and masses, informs our understanding of both models of planet formation and the interior structure of planets that straddle the boundary between sub-Neptunes and super-Earths. The transit radii measured by *Kepler* and the planetary masses measured (or bounded) by radial velocity observations together constrain the interior compositions of Kepler-20b, Kepler-20c, and Kepler-20d, as illustrated by the mass-radius diagram (Figure 12). We employ planet interior structure models (Rogers & Seager 2010; Rogers et al. 2011) to explore the range of plausible planet compositions. The interpretation is challenging because we do not yet know if these sub-Neptune planets had a stunted formation, or if they formed as gas giants and then lost significant mass to evaporation (Baraffe et al. 2004). This is partly owing to the uncertainties involved in atmospheric escape modeling.

Notably, both Kepler-20c and Kepler-20d require significant volatile contents to account for their low mean densities, and cannot be composed of rocky and iron material alone. The volatile material in these planets could take the form of ices (H_2O , CH_4 , NH_3) and/or H/He gas accreted during planet formation. Outgassing of rocky planets releases an insufficient quantity of volatiles (no more than 23% H_2O and 3.6% H_2 relative to the planet mass) to account for Kepler-20c and could account for Kepler-20d only in fine-tuned near-optimal outgassing scenarios (Elkins-Tanton & Seager 2008; Schaefer & Fegley 2008; Rogers et al. 2011). For Kepler-20c, ices (likely dominated by H_2O) would need to constitute the majority of its mass, in the absence of a voluminous, though low-mass, envelope of light gases. Alternatively, a composition with approximately 1% by mass H/He surrounding an Earth-composition refractory interior also matches the observed properties of the planet within 1σ . Intermediate scenarios, wherein both H/He and higher mean molecular weight volatile species from ices contribute to the planet mass, are also possible. For Kepler-20d, the 2σ upper limit on the planet density demands at least a few percent H_2O by mass, or a few tenths of a percent H/He by mass.

The nature of Kepler-20b’s composition is ambiguous: Kepler-20b could be terrestrial (with the transit radius defined by a rocky surface), or it could support a significant gas envelope (like Kepler-20c and Kepler-20d). In the mass-radius diagram (Figure 12), the measured properties of Kepler-20b straddle the pure-silicate composition curve that defines a strict upper bound to rocky planet radii. If Kepler-20b is in fact a terrestrial planet consisting of an iron core surrounded by a silicate mantle, the 1σ limits on the planet mass and radius constrain the iron core to be less than 62% of the planet mass. In particular, an Earth-like composition (30% iron core, 70% silicate mantle) is possible and matches the observational constraints to within 1σ , but a Mercury-like composition (70% iron core,

30% silicate mantle) is not acceptable. Alternatively, Kepler-20b may harbor a substantial gas layer like its sibling planets Kepler-20c and Kepler-20d at larger orbital semi-major axes, and/or contain a significant component of astrophysical ices such as H₂O. The 1 σ lower limits on the planet density constrain the fraction of Kepler-20b’s mass that can be contributed by H₂O ($\lesssim 55\%$) and H/He ($\lesssim 1\%$).

Given their high levels of stellar irradiation (the semi-major axes of all five Kepler-20 planets are smaller than that of Mercury), atmospheric escape likely played an important role sculpting the compositions of the Kepler-20 planets. Planet compositions with low mean molecular weight gas envelopes would be especially susceptible to mass loss. Using a model for energy limited escape from hydrogen-rich envelopes (Lecavelier Des Etangs 2007), we estimate that Kepler-20b would be losing on the order of $4 \times 10^6 \text{ kg s}^{-1}$, which corresponds to $0.02 M_{\oplus} \text{Gyr}^{-1}$. Following the same approach, the estimated hydrogen mass loss rates for Kepler-20c and Kepler-20d are $2 \times 10^6 \text{ kg s}^{-1}$ ($0.01 M_{\oplus} \text{Gyr}^{-1}$) and $8 \times 10^4 \text{ kg s}^{-1}$ ($0.0004 M_{\oplus} \text{Gyr}^{-1}$), respectively. Our theoretical understanding of atmospheric escape from highly irradiated super-Earth and sub-Neptune exoplanets is very uncertain, and higher mass loss rates are plausible (especially at earlier times when the host star was more active). It is intriguing that Kepler-20b, with its shorter orbital period and greater vulnerability to mass loss, also has a higher mean density than Kepler-20c and Kepler-20d. More detailed modeling may constrain Kepler-20b’s compositional history and the extent to which its relative paucity of volatiles can be attributed to evaporation.

The Kepler-20 planetary system shares several remarkable attributes with Kepler-11 (Lissauer et al. 2011b), namely the presence of multiple transiting low-density low-mass planets in a closely spaced orbital architecture. The Kepler-20 system is less extreme than Kepler-11 in the realms of both low planet densities (Figure 12) and dynamical compactness (the Kepler-11 planets exhibit TTVs while the Kepler-20 planets do not).

A striking feature of the Kepler-20 planetary system is the presence of Earth-size rocky planet candidates interspersed between volatile-rich sub-Neptunes at smaller and larger orbital semi-major axes, as also seen in *Kepler* candidate multi-planet systems (Lissauer et al. 2011a). Assuming that both K00070.04 and K00070.05 are planets, the distribution of the Kepler-20 planets in orbital order is as follows: Kepler-20b (3.7 days, $1.9 R_{\oplus}$), K00070.04 (6.1 days, $0.9 R_{\oplus}$), Kepler-20c (10.9 days, $3.1 R_{\oplus}$), K00070.05 (19.6 days, $1.0 R_{\oplus}$), and Kepler-20d (77.6 days, $2.8 R_{\oplus}$). Given the radii and irradiation fluxes of the two Earth-size planet candidates, they would not retain gas envelopes. The first, second, and fourth planets have high densities indicative of solid planets, while the other two planets have low densities requiring significant volatile content. The volatile-rich third planet, Kepler-20c dominates the inner part of the Kepler-20 system, by holding much more mass than the other three inner

planets put together. In the Solar System, the terrestrial planets, gas-giants, and ice giants are neatly segregated in regions with increasing distance from the sun. Planet formation theories were developed to retrodict these Solar System composition trends (e.g., Safronov 1969; Chambers 2010; D’Angelo et al. 2010). In the Kepler-20 system, the locations of the low-density sub-Neptunes that are rich in water and/or gas, and the Earth-size planet candidates does not exhibit a clean ordering with orbital period, challenging the conventional planet formation paradigm. In situ assembly may form multi-planet systems with close-in hot-Neptunes and super-Earths, provided the initial protoplanetary disk contained massive amounts of solids ($\sim 50\text{--}100 M_{\oplus}$) within 1AU of the star (Hansen & Murray 2011).

Kepler was competitively selected as the tenth Discovery mission. Funding for this mission is provided by NASA’s Science Mission Directorate. The authors thank many people who gave so generously of their time to make this mission a success. This work is also based in part on observations made with the *Spitzer Space Telescope*, which is operated by the Jet Propulsion Laboratory, California Institute of Technology under a contract with NASA. Support for this work was provided by NASA through an award issued by JPL/Caltech. We would like to thank the *Spitzer* staff at IPAC and in particular Nancy Silbermann for scheduling the Spitzer observations of this program. Some of the data presented herein were obtained at the W. M. Keck Observatory, which is operated as a scientific partnership among the California Institute of Technology, the University of California and the National Aeronautics and Space Administration. The Observatory was made possible by the generous financial support of the W. M. Keck Foundation. (c) 2011 all rights reserved.

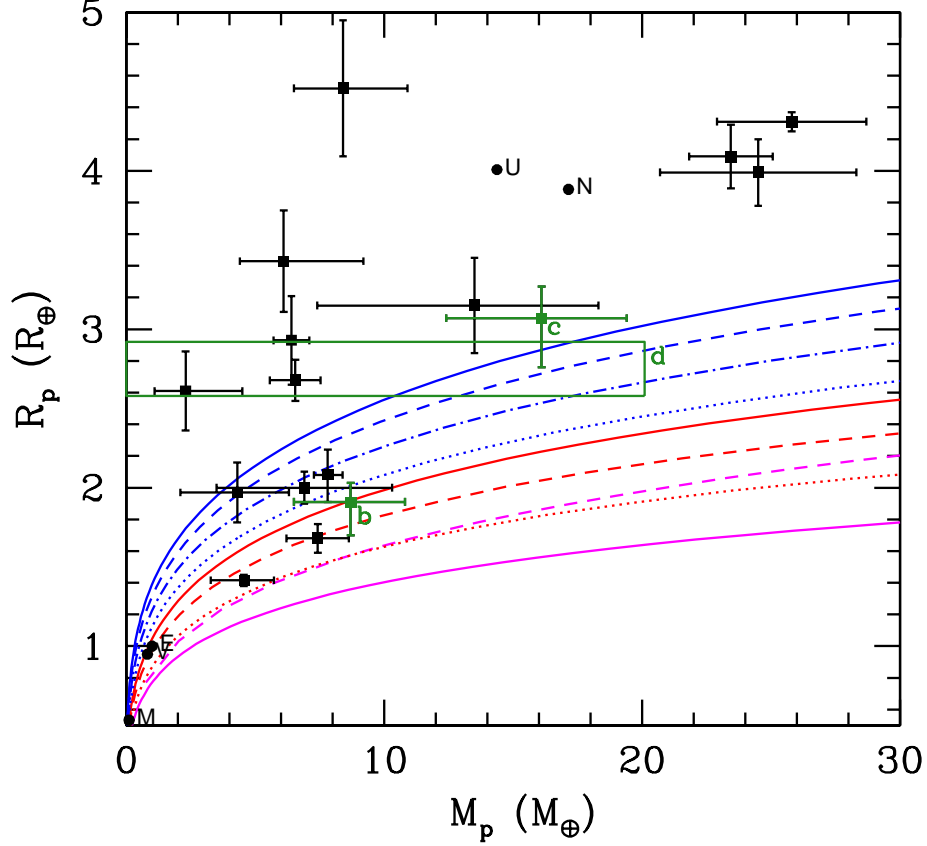


Fig. 12.— Mass-radius relationships of small transiting planets. The three confirmed planets in the Kepler-20 system are highlighted in green. Kepler-20b and Kepler-20c are plotted with error bars delimiting the 1σ uncertainties on the planet mass and radius, while Kepler-20d is plotted with bands illustrating the 2σ mass upper limit. Other small transiting exoplanets with measured masses (Kepler-10b, CoRoT-7b, Kepler-11bcdef, Kepler-18b, 55Cnc e, GJ 1214b, HD 97658b, GJ 436b, Kepler-4b, HAT-P-11b) are plotted in black. The Solar System planets are indicated with the first letters of their names. The curves are illustrative constant-temperature (300 K) mass-radius relations for bodies devoid of H/He from Seager et al. (2007). The solid lines are homogeneous-composition planets: water ice (blue solid), MgSiO_3 perovskite (red solid), and iron (magenta solid). The non-solid lines are mass-radius relations for differentiated planets: 75% water ice, 22% silicate shell, and 3% iron core (blue dashed); Ganymede-like with 45% water ice, 48.5% silicate shell, and 6.5% iron core (blue dot-dashed); 25% water ice, 52.5% silicate shell, and 22.5% iron core (blue dotted); Earth-like with 67.5% silicate mantle and 32.5% iron core (red dashed); and Mercury-like with 30% silicate mantle and 70% iron core (red dotted). The minimal radius curve based on simulations of collisional mantle stripping from differentiated silicate-iron planets (Marcus et al. 2010) is denoted by the dashed magenta line.

REFERENCES

- Adams, E. R., Seager, S. & Elkins-Tanton, L. 2008, *ApJ*, 673, 1160
- Agol, E., Steffen, J., Sari, R., & Clarkson, W. 2005, *MNRAS*, 359, 567
- Ballard, S., Fabrycky, D., Fressin, F., et al. 2011, *ApJ*, in press, arXiv:1109.1561
- Baraffe, I., Selsis, F., Chabrier, G., et al. 2004, *A&A*, 419, L13
- Basri, G., Walkowicz, L. M., Batalha, N., et al. 2010, *ApJ*, 713, L155
- Basri, G., Walkowicz, L. M., Batalha, N., et al. 2011, *AJ*, 141, 20
- Batalha, N. M., Rowe, J. F., Gilliland, R. L., et al. 2010, *ApJ*, 713, L103
- Batalha, N. M., Borucki, W. J., Bryson, S. T., et al. 2011, *ApJ*, 729, 27
- Borucki, W. J., Koch, D., Basri, G., et al. 2010, *Science*, 327, 977
- Borucki, W. J., Koch, D. G., Basri, G., et al. 2011, *ApJ*, 736, 19
- Brown, T. M., Latham, D. W., Everett, M. E., & Esquerdo, G. A. 2011, *AJ*, 142, 112
- Bryson, S. T., Tenenbaum, P., Jenkins, J. M., et al. 2010, *ApJ*, 713, L97
- Buchhave, L. A., Bakos, G. Á., Hartman, J. D., et al. 2010, *ApJ*, 720, 1118
- Buchhave, L. A., Latham, D. W., Carter, J. A., et al. 2011, *ApJS*, 197, 3
- Butler, R. P., Marcy, G. W., Fischer, D. A., et al. 1999, *ApJ*, 526, 916
- Caldwell, D. A., Kolodziejczak, J. J., Van Cleve, J. E., et al. 2010, *ApJ*, 713, L92
- Chambers, J. E. 1999, *MNRAS*, 304, 793
- Chambers, J. 2010, *Exoplanets*, 297
- Charbonneau, D., Brown, T. M., Latham, D. W., & Mayor, M. 2000, *ApJ*, 529, L45
- Charbonneau, D., Brown, T. M., Noyes, R. W. & Gilliland, R. L. 2002. *ApJ*, 568, 377
- Charbonneau, D., Allen, L. E., Megeath, S. T., et al. 2005, *ApJ*, 626, 523
- Claret, A., & Bloemen, S. 2011, *A&A*, 529, A75
- Cochran, W. D., Fabrycky, D. C., Torres, G., et al. 2011, *ApJS*, 197, 7

- D'Angelo, G., Durisen, R. H., & Lissauer, J. J. 2010, *Exoplanets*, 319
- Demarque, P., Woo, J.-H., Kim, Y.-C., & Yi, S. K. 2004, *ApJS*, 155, 667
- Désert, J.-M., Lecavelier des Etangs, A., Hébrard, G., Sing, D. K., Ehrenreich, D., Ferlet, R., & Vidal-Madjar, A. 2009, *ApJ*, 699, 478
- Désert, J.-M., Sing, D., Vidal-Madjar, A., et al. 2011a, *A&A*, 526, A12
- Désert, J.-M., Charbonneau, D., Fortney, J. J., et al. 2011b, *ApJS*, 197, 11
- Djupvik, A. A., & Andersen, J. 2010, *Highlights of Spanish Astrophysics V*, 211
- Elkins-Tanton, L. T., & Seager, S. 2008, *ApJ*, 685, 1237
- Fazio, G. G., Hora, J. L., Allen, L. E., et al. 2004, *ApJS*, 154, 10
- Ford, E. B., Lystad, V. & Rasio, F. A. 2005, *Nature*, 434, 873
- Ford, E. B., Rowe, J. F., Fabrycky, D. C., et al. 2011, *ApJS*, 197, 2
- Fressin, F., Torres, G., Désert, J.-M., et al. 2011a, *ApJS*, 197, 5
- Fressin, F., Torres, G., Pont, F., et al. 2011b, *ApJ*, accepted, arXiv:1110.5336
- Fressin, F., Torres, G., Rowe, J. F., et al. 2012, *Nature*, accepted
- Gilliland, R. L., Jenkins, J. M., Borucki, W. J., et al. 2010, *ApJ*, 713, L160
- Gregory, P. C. 2011, *MNRAS*, 410, 94
- Hansen, B. M. S. & Murray N. 2011, arXiv:1105.2050
- Hayward, T. L., Brandl, B., Pirger, B., Blacken, C., Gull, G. E., Schoenwald, J., & Houck, J. R. 2001, *PASP*, 113, 105
- Henry, G. W., Marcy, G. W., Butler, R. P., & Vogt, S. S. 2000, *ApJ*, 529, L41
- Holman, M. J., & Murray, N. W. 2005, *Science*, 307, 1288
- Holman, M. J., Fabrycky, D. C., Ragozzine, D., et al. 2010, *Science*, 330, 51
- Horch, E. P., Gomez, S. C., Sherry, W. H., Howell, S. B., Ciardi, D. R., Anderson, L. M. & van Altena, W. F. 2011, *AJ*, 141, 45
- Howell, S. B. et al. 2011a, *ApJ*, submitted

- Howell, S. B., Everett, M. E., Sherry, W., Horch, E., & Ciardi, D. R. 2011b, *AJ*, 142, 19
- Isaacson, H., & Fischer, D. 2010, *ApJ*, 725, 875
- Jenkins, J. M., Caldwell, D. A., Chandrasekaran, H., et al. 2010a, *ApJ*, 713, L87
- Jenkins, J. M., Caldwell, D. A., Chandrasekaran, H., et al. 2010b, *ApJ*, 713, L120
- Jenkins, J. M., Borucki, W. J., Koch, D. G., et al. 2010c, *ApJ*, 724, 1108
- Jenkins, J. M., J. C. Smith, P. Tenenbaum, J. D. Twicken, and Van Cleve, J. 2011, in *Advances in Machine Learning and Data Mining for Astronomy* (eds. M. Way, J. Scargle, K. Ali, A. Srivastava), Chapman and Hall/CRC Press
- Johnson, J. A., Clanton, C., Howard, A. W. et al. 2011, *ApJS*, 197, 26
- Knutson, H. A. et al. 2007, *Nature*, 447, 183
- Knutson, H. A., Charbonneau, D., Allen, L. E., Burrows, A., & Megeath, S. T. 2008, *ApJ*, 673, 526
- Koch, D. G., Borucki, W. J., Basri, G., et al. 2010, *ApJ*, 713, L79
- Kokubo, E., Yoshinaga, K., & Makino, J. 1998, *MNRAS*, 297, 1067
- Latham, D. W., Rowe, J. F., Quinn, S. N., et al. 2011, *ApJ*, 732, L24
- Lecavelier Des Etangs, A. 2007, *A&A*, 461, 1185
- Lee, M. H. & Peale, S. J. 2002, *ApJ*, 567, 596
- Lissauer, J. J., Ragozzine, D., Fabrycky, D. C., et al. 2011a, *ApJS*, 197, 8
- Lissauer, J. J., Fabrycky, D. C., Ford, E. B., et al. 2011b, *Nature*, 470, 53
- Lloyd, J. P., Liu, M. C., Macintosh, B. A., Sevenson, S. A., Deich, W. T. S. & Graham, J. R. 2000, *Proc. SPIE*, 4008, 814
- Malhotra, R. 2008, *ApJ*, 575, L33
- Mamajek, E. E., & Hillenbrand, L. A. 2008, *ApJ*, 687, 1264
- Mandel, K., & Agol, E. 2002, *ApJ*, 580, L171
- Marcus, R. A., Sasselov, D., Hernquist, L., & Stewart, S. T. 2010, *ApJ*, 712, L73

- Mayor, M., Marmier, M., Lovis, C., et al. 2011, arXiv1109.2497
- Miller, N. & Fortney, J. J. 2011, ApJ, 736, L29
- Morton, T. D. & Johnson, J. A. 2011, ApJ, 738, 170
- Noyes, R. W., Hartmann, L. W., Baliunas, S. L., Duncan, D. K., & Vaughan, A. H. 1984, ApJ, 279, 763
- Rasio, F. A., Nicholson, P. D., Shapiro, S. L. & Teukolsky, S. A. 1992, Nature, 355, 325
- Reach, W. T., et al. 2006, IRAC Data Handbook v3.0
- Robin, A. C., Reylé, C., Derrière, S., & Picaud, S. 2003, A&A, 409, 523
- Rogers, L. A., & Seager, S. 2010b, ApJ, 716, 1208
- Rogers, L. A., Bodenheimer, P., Lissauer, J. J., & Seager, S. 2011, ApJ, 738, 59
- Safronov, V. S. 1969, Evoliutsiia doplanetnogo oblaka, Nauka, Moscow
- Schaefer, L., & Fegley, B. 2008, Meteoritics and Planetary Science Supplement, 43, 5037
- Seager, S., Kuchner, M., Hier-Majumder, C. A., & Militzer, B. 2007, ApJ, 669, 1279
- Slawson, R. W., Prša, A., Welsh, W. F., et al. 2011, AJ, 142, 160
- Steffen, J. H., Batalha, N. M., Borucki, W. J., et al. 2010, ApJ, 725, 1226
- Ter Brakk, C. J. F. 2006, Statistical Computing, 16, 239
- Torres, G., Neuhäuser, R., & Guenther, E. W. 2002, AJ, 123, 1701
- Torres, G., Konacki, M., Sasselov, D. D., & Jha, S. 2004, ApJ, 614, 979
- Torres, G., Fressin, F., Batalha, N. M., et al. 2011, ApJ, 727, 24
- Triaud, A. H. M. J. et al. 2010 å, 524, 25
- Troy, M., et al. 2000, Proc. SPIE, 4007, 31
- Valenti, J. A. & Piskunov, N. 1996, A&A, 118, 595
- Valenti, J. A. & Fischer, D. A. 2005, ApJS, 159, 141
- Van Cleve, J., & Caldwell, D. A. 2009, Kepler Instrument Handbook, KSCI 19033-001. Moffett Field, CA: NASA Ames Research Center

Vogt, S. S., Allen, S. L., Bigelow, B. C., et al. 1994, Proc. SPIE, 2198, 362

Werner, M. W., Roellig, T. L., Low, F. J., et al. 2004, ApJS, 154, 1

Winn, J. N. 2010, in *Exoplanets* (ed. S. Seager), pp. 55

Wisdom, J., & Holman, M. 1991, AJ, 102, 1528

Wolszczan, A. & Frail, D. A. 1992, Nature, 355, 145

Wolszczan, A. 1992, Science, 264, 538

Yi, S., Demarque, P., Kim, Y.-C., et al. 2001, ApJS, 136, 417